Dynamics of live oil droplets and natural gas bubbles in deep water

–

Supporting Information

Authors: Jonas Gros,[a,*] J. Samuel Arey,[b] Scott A. Socolofsky,[c] and Anusha L. Dissanayake[d,1]

[a] RD2/Marine Geosystems, GEOMAR Helmholtz Centre for Ocean Research Kiel, Wischhofstrasse 1-3, D-24148 Kiel, Germany

[b] ExxonMobil Biomedical Sciences Inc., Annandale, New Jersey 08801, United States

[c] Zachry Department of Civil Engineering, Texas A&M University, College Station, Texas 77843, United States

[d] RPS Ocean Science, South Kingstown, Rhode Island 02879, United States

[1] present address: SINTEF Ocean, 7465 Trondheim, Norway

* Corresponding author. Email: jogros@geomar.de. Phone: +49 431 600 2267.

This document provides: Extended description of the TAMOC model (section S1); assumptions for the simulations of the *Deepwater Horizon* near-field on June 8, 2010 (section S2); assumptions for the simulation of live oil droplets and gas bubbles in the sea (section S3); quantitative evaluation of the phases driving mass transfer limitation (section S4); discussion of gas supersaturation in the vessel water of the experimental device of Pesch et al.[1] (section S5); graphics of TAMOC simulation of experiments 1–3 of Pesch et al.[1] with suppressed aqueous dissolution of methane (section S6); graphics of TAMOC simulation of experiments 4–6 (section S7) and 10–12 of Pesch et al.[1] (section S8); live and dead oil droplet ascent velocities (section S9); predicted vertical velocity of the plume during *Deepwater Horizon* (section S10); discussion of why the conditions selected for the experiments of Pesch et al.[1] favored ebullition of the live oil droplets (section S11); and comparison of phase behaviors for single-component versus multicomponent fluids and simulated phase envelopes (section S12).
38 pages; 5 tables; 13 figures.

S1 Extended description of the TAMOC model and underlying equations

This section provides a general description of the formulas used in TAMOC. The reader is referred to previous work for in-depth description[2–5] and validation[2–9] of the TAMOC model, and to the main text and sections S2 and S3 for description of the choice of model setup and boundary conditions used for the simulations reported in this article. The normal TAMOC code is freely available on-line, and the latest version can be downloaded at: https://github.com/socolofs/tamoc. The simulations reported in the present article used TAMOC model versions that were slightly modified from TAMOC version 0.1.17. The TAMOC versions used in the present article are publicly available at https://doi.org/10.7266/PSTFE3GN (TAMOC version used to simulate the Pesch et al.[1] laboratory experiments) and at https://doi.org/10.7266/N7DF6P8R (TAMOC version used to simulate the *Deepwater Horizon*, section S2, and the releases of gas bubbles and oil droplets at varied water depths, section S3).

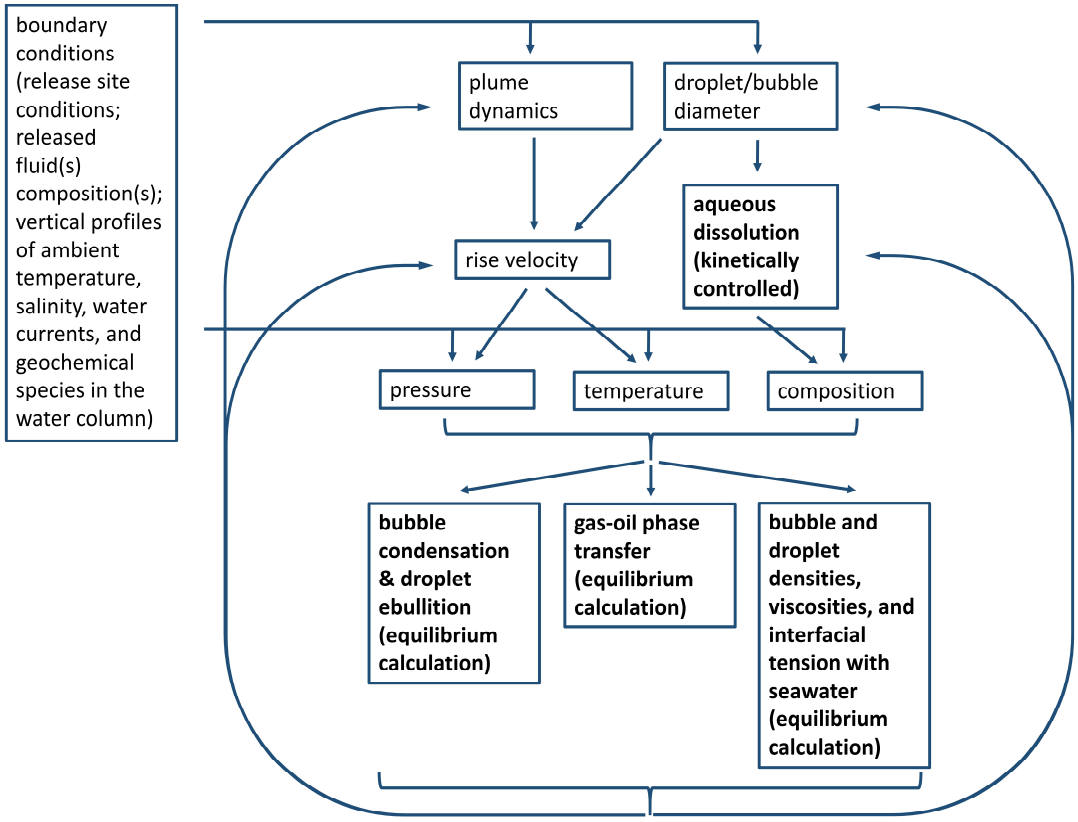

Figure S1. Schematic of the coupled processes simulated in TAMOC with a focus on chemical mass transfer and thermodynamic phenomena in the water column. The schematics also describes which processes are assumed fast enough that they can be simulated through equilibrium calculations and which processes are assumed to be kinetically controlled (whose kinetics are simulated), based on calculations described in section S4.

In TAMOC, the rates of mass transfer of individual petroleum compounds and pseudo-components from droplets, bubbles, or two-phase droplet-bubble pairs into seawater follow a kinetic expression:[10]

$$\frac{dm_i}{dt} = -A \cdot \beta_i \cdot \left(C_{w,i}^{eq} - C_{w,i}\right) \quad \text{(S1)}$$

where m_i is the total mass of component *i* in the droplet, bubble, or droplet-bubble pair; *A* is the surface area of the droplet, bubble, or droplet-bubble pair; β_i is the mass transfer coefficient (units: length time^{-1}) of component *i* at the fluid particle-water interface (here, a fluid particle is either a droplet, a bubble, or a two-phase droplet-bubble pair); $C_{w,i}^{eq}$ is the equilibrium aqueous concentration of component *i* based on partitioning equilibrium with the droplet, bubble, or either of the phases of a droplet-bubble pair, calculated from the pressure-dependent, temperature-dependent, and salinity-dependent Henry's law constant[11–15] and petroleum phase fugacities computed from the Peng–Robinson equation of state (PR EOS) with the 1978 modification;[3,16–19] and $C_{w,i}$ is the modeled aqueous concentration of component *i* in the seawater adjacent to the droplet, bubble, or droplet-bubble pair.

The text describes the two attached phases as a "droplet-bubble pair". This shall not be taken to mean two separated entities. Rather, as stated in the main text, the model assumes a single entity (as observed in the laboratory by Pesch et al.,[1] Figure 1b), where the gas (top) and oil (bottom) form two spherical caps. The conditions both in the laboratory and in the field may diverge from the idealized model representation. This assumption only affects the calculated interfacial tension between the droplet-bubble pair and the seawater used in the simulations (discussed below), whereas other properties are unaffected by the assumed disposition of the gas and liquid phases within the droplet-bubble pair.

Properties of droplets, bubbles, or two-phase droplet-bubble pairs—including shape, surface area, slip velocity, and β_i—are calculated based on formulas by Clift et al.,[20] with the exception of β_i for components in liquid droplets[21] and circulating bubbles,[22] as explained below.

The shapes of droplets, bubbles, and two-phase droplet-bubble pairs depend on the Eotvos number (*Eo*), Morton number (*M*), and the "*H* parameter": *Eo*, *M*, and *H* are given by:

$$Eo = \frac{g \cdot \left(\rho_{water} - \rho_{particle}\right) \cdot d_{particle}^{2}}{\sigma_{particle\ /\ water}} \quad \text{(S2)}$$

where *g* is the gravitational acceleration, ρ_{water} is the density of seawater and is calculated using formulas from Gill,[23] $\sigma_{particle/water}$ is the interfacial tension between the droplet, bubble, or droplet-bubble pair and seawater, $\rho_{particle}$ is the density of the droplet, bubble, or droplet-bubble pair, and $d_{particle}$ is the equivalent spherical diameter of the droplet, bubble, or droplet-bubble pair:

$$d_{particle} = \left(\frac{6 \cdot V_{particle}}{\pi}\right)^{1/3} \quad \text{(S3)}$$

where $V_{particle}$ the volume of the droplet, bubble, or droplet-bubble pair.

The Morton number is given by:

$$M = \frac{g \cdot \mu_{water}^4 \cdot \left(\rho_{water} - \rho_{particle}\right)}{\rho_{water}^2 \cdot \sigma_{particle/water}^3} \quad \text{(S4)}$$

where μ_{water} is the dynamic viscosity of seawater at given conditions of temperature, salinity,[24] and pressure.[25]

The H parameter is given by:

$$H = \frac{4}{3} \cdot Eo \cdot M^{-0.149} \cdot \left(\frac{\mu_{water}}{0.0009}\right)^{-0.14} \quad \text{(S5)}$$

The shape of the bubble is assumed spherical if $H<2$; ellipsoidal if $2 \leq H < 1000$, $Eo<40$, and $M<0.001$; and a spherical cap otherwise. Based on the estimated shape, the surface area is calculated from the model sketched on Figure 8.1 on page 204 of the book by Clift et al.[20] for spherical-cap fluid particles. The surface area of an ellipsoidal or spherical fluid particle is calculated as the area of the volume-equivalent sphere.

Slip velocities (i.e. the rise velocity relative to surrounding water), u_{slip}, of spherical-cap fluid particles depend on ρ_{water}, $\rho_{particle}$, and $d_{particle}$ based on equation 8-11 on page 206 of Clift et al.;[20] u_{slip} of spherical fluid particles additionally depend on μ_{water} based on equations 5-15 and 2-16 and Table 5.3 on pages 113, 114, and 26 of Clift et al.[20] The u_{slip} values of ellipsoid fluid particles further depend on $\mu_{particle}$ (the dynamic viscosity of the fluid particle), weakly on $\sigma_{particle/water}$, and also whether the fluid particle has a circulating or non-circulating interface, based on equations on pages 175–178 of Clift et al.[20] The total velocities of fluid particles depend on the resultant of their local vertical slip velocities and the local velocity vector of the plume in which the particles may be situated. The β_i value is obtained from a combination of formulas, depending on the cases explained in Table S1.

Table S1. Description of formulas used to estimate mass transfer coefficients, β_i. The term D_i is the diffusion coefficient of the petroleum component *i* in water, calculated with the Hayduk–Laudie[26] formula (eq. S6) in TAMOC

Shape of the droplet, bubble, or droplet-bubble pair	Is the droplet, bubble, or droplet-bubble pair >50% gas by volume?	Does the droplet, bubble, or droplet-bubble pair have a circulating interface?	Reference for formulas used	Properties on which the mass transfer coefficient is assumed to depend	Comment
sphere or ellipsoid	yes	yes	Johnson et al.[22] or Clift et al.[20]	u_{slip}, $d_{particle}$, D_i or u_{slip}, ρ_{water}, $d_{particle}$, μ_{water}, D_i	Uses the largest value between Johnson et al. and Clift et al. methods. Uses equation 42 of Johnson et al. For Clift et al.: For Re < 1, uses equation (3-49) on page 49 for creeping flow past a sphere. For Re < 100, equation (5-25) on page 121 is used; for Re < 1e5, equations in Table 5.4 on page 123 are used.
	yes	no	Clift et al.[20]	u_{slip}, ρ_{water}, $d_{particle}$, μ_{water}, D_i	For Re < 1, uses equation (3-49) on page 49 for creeping flow past a sphere. For Re < 100, equation (5-25) on page 121 is used; for Re < 1e5, equations in Table 5.4 on page 123 are used.
	no	yes	Kumar and Hartland[21]	u_{slip}, ρ_{water}, $d_{particle}$, $\sigma_{particle/water}$, μ_{water}, $\mu_{particle}$, D_i	
	no	no	Clift et al.[20]	u_{slip}, ρ_{water}, $d_{particle}$, μ_{water}, D_i	For Re < 1, uses equation (3-49) on page 49 for creeping flow past a sphere. For Re < 100, equation (5-25) on page 121 is used; for Re < 1e5, equations in Table 5.4 on page 123 are used.
spherical cap	yes	yes	Johnson et al.[22]	u_{slip}, $d_{particle}$, D_i	Uses equation 42 of Johnson et al.
	yes	no	Clift et al.[20]	u_{slip}, ρ_{water}, $\rho_{particle}$, $d_{particle}$, μ_{water}, D_i	equation (8-28) on page 214
	no	yes	Johnson et al.[22]	u_{slip}, $d_{particle}$, D_i	Uses equation 42 of Johnson et al.
	no	no	Clift et al.[20]	u_{slip}, ρ_{water}, $\rho_{particle}$, $d_{particle}$, μ_{water}, D_i	equation (8-28) on page 214

TAMOC estimates the dynamic viscosities of petroleum liquid and gas phases based on the Pedersen et al. method for light oils.[3,19,27] The liquid-seawater and gas-seawater interfacial tensions are calculated with the method of Firoozabadi and Ramey.[28,29] The modeled dynamic viscosities and interfacial tensions depend on fluid particle composition, pressure, and temperature conditions. The parameter β_i is assumed to depend on the temperature-dependent diffusion coefficient of the petroleum compound in water, D_i, which is calculated with the Hayduk–Laudie formula:[26]

$$D_i(T) = \frac{13.26 \cdot 10^{-9}}{\left(\eta(T) \cdot 10^3\right)^{1.14} \cdot \left(\overline{V}_{bp,i} \cdot 10^6\right)^{0.589}} \tag{S6}$$

where: D_i has units of m s^{-2}; η is the temperature-dependent dynamic viscosity of seawater,[24] in Pa s; and $\overline{V}_{bp,i}$ is the molar volume of the solute at its normal boiling point, in m^3 mol^{-1}. The $\overline{V}_{bp,i}$ values were taken from literature data when available;[26] when unavailable, TAMOC estimates $\overline{V}_{bp,i}$ from the critical molar volume, $V_{c,i}$, according to the Tyn and Calus formula:[30]

$$\overline{V}_{bp,i} = 0.285 \cdot \left(V_{c,i} \cdot 10^6\right)^{1.048} \cdot 10^{-6} \tag{S7}$$

where both $\overline{V}_{bp,i}$ and $V_{c,i}$ are expressed in m^3 mol^{-1}. Eqs. S6 and S7 include some modified coefficients compared to the traditional way of writing them that may be unfamiliar to some readers; these coefficients arise purely from the arithmetic needed to convert the relations to base units of the International Unit System.

In the simulation of two-phase droplet-bubble pairs, the model assumes that the effective interfacial tension between a droplet-bubble pair and seawater is given by a weighted average of the liquid-phase and gas-phase interfacial tensions with seawater, using the equivalent spherical surface area as the weighting factor. It is difficult to unambiguously assign a proper value to the interfacial tension with seawater for a two-phase droplet-bubble pair, and the choice made here enables a smooth transition of the model between oil-seawater values for 100% liquid droplets up to gas-seawater values for 100% gas bubbles. The sensitivity of the simulations to this choice is very small and this choice does not affect any conclusions made in the present study, as discussed at the end of this section.

The effective density of a two-phase droplet-bubble pair is given by:

$$\rho_p = \frac{m_{gas} + m_{liq}}{V_{gas} + V_{liq}} \tag{S8}$$

where ρ_p is the effective density of the two-phase droplet-bubble pair, m_{liq} and m_{gas} are the masses of liquid and gas phases, respectively, and V_{liq} and V_{gas} are the corresponding volumes of each phase, as predicted by TAMOC assuming thermodynamic equilibrium between the oil and gas phases.

In response to the query of one reviewer, we considered the possibility that the gas-seawater interface could be assigned the value given by the liquid-seawater interfacial tension, due to the possible influence of an oil film at the bubble-water interface. For droplets, bubbles, or two-phase droplet-bubble pairs having a non-circulating interface, the only property depending directly on $\sigma_{particle/water}$ in the model is the slip velocity for those droplets that are in the ellipsoid shape range (0.8–18 mm diameter droplets for LSC live oil at 151 bar and 20°C), and mass transfer rate in turn depends on the slip velocity (Table S1). For oil droplets, if we consider the limiting cases in which the slip velocity is calculated based on either the estimated gas-water interfacial tension or the estimated oil-water interfacial tension, we find an average absolute deviation in slip velocity of 11% (over the range of considered diameters, 0.8–18 mm). This would produce an average absolute deviation in methane mass transfer coefficient of 13% (over the range of considered diameters, 0.8–18 mm).

In order to assess the sensitivity of the results reported in the present study to this assumption, we recalculated some of the results presented in the main text, assuming the oil-seawater interfacial tension value for droplet-bubble pairs instead of the procedure described above (weighted average of the liquid-phase and gas-phase interfacial tensions with seawater, using the equivalent spherical surface area as the weighting factor, as described above). Simulations reported in Figure 5 of the main text are barely affected by the choice of one or the other assumption (Figures 5 and S2). Similarly, the reported results of the simulations of the laboratory experiments by Pesch et al.[1] remain unchanged within the number of significant digits displayed in Table 1 in the main text.

This analysis indicated that the choice of interfacial tension of two-phase droplet-bubble pairs (modeled as either an oil-seawater value or a weighted average value based on the oil-seawater and gas-seawater values) is negligible in driving the simulation outcome. However, interfacial tension with seawater remains a key property in other contexts. In particular, interfacial tension with seawater was shown by previous studies[31–34] to be key in determining the size of droplets and bubbles experiencing turbulent break-up in a jet.

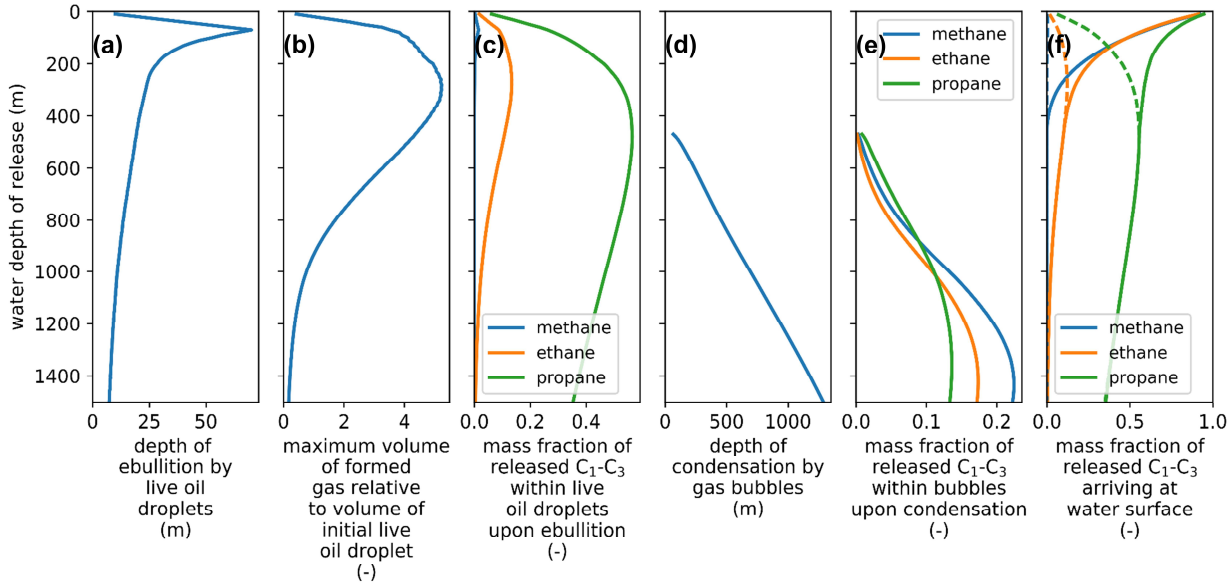

Figure S2. Redrawn figure reporting the same simulations as on Figure 5 in the main text, except that the oil-seawater interfacial tension was used for any droplet-bubble pair, instead of our selected procedure. Comparison with Figure 5 in main text indicates that this different assumption has negligible effects on simulation outcomes. Refer to the Figure 5 in main text for detailed figure caption.

S2 Simulation of the *Deepwater Horizon* near-field on June 8, 2010

This section describes the assumptions that were made for simulations of the *Deepwater Horizon* disaster. In a previous study,[2] we simulated the situation prevailing during one of the days of the *Deepwater Horizon*, June 8, 2010, which we assumed to be representative of the post-riser cut period of this oil spill. These simulations were validated to field data[35–37] in that previous work.[2] In a separate study, the thermodynamics model[3] and the selected composition MC_1[3,37] of 279 chemical components describing the released Macondo reservoir fluid were shown to predict well the properties of the whole Macondo reservoir fluid under relevant pressure and temperature conditions.[3] A phase diagram of the Macondo reservoir fluid was published previously.[3] We assumed a thermodynamic-equilibrium separation of the Macondo reservoir fluid[37] into gas and liquid petroleum phases at the ambient conditions (153 bar and 4.3°C) prevailing at the 1,505-m release water depth. Model boundary conditions were parameterized based on environmental and technical data measured for June 8, 2010, which included subsea dispersant injection at the wellhead.[2] The simulations include buoyant-plume dynamics, in agreement with field observations.[38] Assumed seawater temperature and salinity profiles are reported in Figure S3b,c and used again in the present article as representative water column data (see section S3). The reader is referred to section S1 and previous work[2–5] for further description of the model and to previous work[2] for the assumed initial droplet and bubble size distributions.

TAMOC fully couples the processes of gas-oil partitioning, gas-oil phase transitions (ebullition and condensation), aqueous dissolution kinetics, and buoyant plume dynamics, all of which have been shown to contribute importantly to the fate of oil and gas in the *Deepwater Horizon* near-field. Several lines of evidence support the conclusion that the model enables useful inferences about *Deepwater Horizon*, as

well as predictions for other scenarios involving underwater release of oil and gas. Nonetheless, the assumptions employed in any such model are necessarily a simplification of these highly complex events. We have carefully considered some key simplifications, which we discuss briefly below.

The present study tracks the dynamics of the oil droplets after they have completed primary breakup and are rising through a medium of entrained seawater. Pesch et al. (2020)[39] have postulated effects caused by the pressure drop at the wellhead that may affect droplet formation or the oil and gas composition at the end of the primary breakup zone. However, this postulated pressure drop remains unconstrained over the orifice itself. Pressure was observed to drop dramatically within the 16.4-m-long[40] blowout preventer of the *Deepwater Horizon*,[41] but the pressure drop across the orifice on June 8, 2010 remains unknown. Independently of other potential effects, we report here the effect of the pressure and temperature drops on the gas and liquid repartition of petroleum fluids at thermodynamic equilibrium. The petroleum fluids were already well into the two phase region below the failed blowout preventer where the fluids were 31% gas by volume (assuming equilibrium at 378.15 K and 240 bar[3]), and experienced rapid decompression to ambient deep-sea pressure, combined with a temperature decrease over the first few meters immediately above the orifice,[3,37] such that the fluids were 29% gas by volume at ambient seawater conditions (assuming equilibrium at 277.45 K and 153 bar).[2,3] Overall, 18% of the gas mass condensed between these two locations, which are separated by a distance of approximately 20–25 m, based on equation-of-state calculations. The volume flow rates of released gas and oil out of the orifice are believed to also influence the initial droplet and bubble sizes.[31–34] Because of the good agreement obtained between model predictions and field observations reported by Gros et al. (2017),[2] we follow their approach and assume a live-oil composition at the end of the breakup zone in equilibrium with local ambient conditions (Gros et al. 2017).[2] This computed equilibrium oil and gas composition is used as input to the VDROP-J model[32] for predicting the initial size distributions of gas bubbles and oil droplets. In the sensitivity study reported in Figure 4, we consider the behavior of various droplet sizes.

The present study assumes that at the emission source, complete separation of gas and oil phases occurred. Despite that this assumption was broadly applied in the literature,[2,40,42–44] there is unfortunately insufficient data to test this hypothesis for realistic field conditions (the high turbulence level immediately above the *Deepwater Horizon* wellhead). Two-phase gas-oil[1,39] and water-oil[45] droplets can be generated in the laboratory, however compositional field data at a natural seep at 3,400 m water depth seemed to indicate partial to total separation between gas and live oil at the emission source.[46]

S3 Simulation of the behaviors of live oil droplets and gas bubbles in deep water

To evaluate the importance of phase transitions under varied environmental conditions, we simulated individual C_1–C_3-saturated oil droplets and gas bubbles released at different water depths. In these simulations, we used profiles of temperature, salinity, and oxygen concentration measured in the Gulf of Mexico,[2] and we assumed a nitrogen profile at equilibrium with the atmosphere[47] (Figure S3). Buoyant plume dynamics were not included in these model simulations. These scenarios therefore represent the near-field conditions often encountered at natural seeps or possibly encountered at some types of small-

scale releases at active or abandoned extraction or exploration infrastructures, which would generate weak bubble plumes[48] leading to limited vertical acceleration of bubbles and droplets.

At each release depth, we assumed an initial gas-liquid phase separation of a petroleum mixture that is thermodynamically equilibrated at local conditions, which provided the compositions of both a gas phase and a live oil phase. We then simulated the separate behaviors of single gas bubbles and single live oil droplets, assuming dirty interfaces in both cases. The simulated petroleum fluid was parameterized to represent LSC dead oil mixed with methane, ethane, and propane at mole fractions of 0.834, 0.099, 0.067, respectively. The total mass fraction (0.235) of C_1–C_3 in the petroleum mixture was chosen to mimic the composition of the Macondo reservoir fluid[37] released during the *Deepwater Horizon* oil spill, assuming a local unitless gas-to-oil volume ratio of 0.4 at 1500-m water depth.[3] We simulated the behavior of single live oil droplets and single live gas bubbles having initial diameters of 5 mm as an example scenario. This size was likely similar to the sizes of droplets and bubbles that would have formed above the Macondo wellhead during June 8, 2010, in the absence of subsea dispersant injection, based on VDROP-J[32] simulations.[2] However, droplets and bubbles of this size could also arise from a quiescent natural seep[49,50] or from a smaller release (such as possibly some releases through orifices with slow exit velocity of the leaked fluids or a small leak oozing through the seabed sediments). The natural gas composition[37] simulated here lies within the range of reported compositions for petroleum reservoirs,[25,51] which are usually dominated by methane for the C_1–C_3 fraction (by mole).

We briefly investigated whether the presence of C_1–C_3 compounds in the ambient water column may affect aqueous dissolution dynamics of oil droplets or gas bubbles. Methane (C_1), ethane (C_2), and propane (C_3) were assumed absent (concentration = 0 kg m^{-3}) in the ambient water column. Based on eq. S1, this assumption is found to affect the simulated behaviors of deep-sea live oil droplets and bubbles by <0.01%. Even the elevated methane concentrations found close to natural gas venting sites[46] or in land-locked anoxic basins[52] do not exceed 30 µM (or about 4 orders of magnitude higher than the concentration at equilibrium with the current atmospheric methane concentration of ~2 ppmv); these unusually high methane concentrations would reduce the rate of aqueous dissolution of a pure-methane bubble by 2% at a 1-m water depth, 1% at a 10-m water depth, or 0.1% at a 200-m water depth. In the event that elevated concentrations of methane or any other light molecule would nevertheless be present within a water body or experimental vessel, the model is suited to handle such cases, by assigning a non-zero ambient aqueous concentration for the relevant gases, which could potentially influence mass transfer kinetics and thus gas transport through the water column. In previous work,[19] we evaluated the role of ambient dissolved N_2 and O_2 present in the water column at the Macondo well site, and we found that these dissolved species had a negligible influence on deep-sea behavior of methane, ethane, propane, and other light molecules during the *Deepwater Horizon* disaster. (This contrasts with the conditions within the closed vessel, having a fixed seawater volume, used for the Pesch et al.[1] laboratory experiments. For these cases we find that the fully simulated dynamically-evolving seawater concentrations of dissolved species including methane significantly affect mass transfer, as further discussed in the main text and Supporting Information sections S5 and S11.)

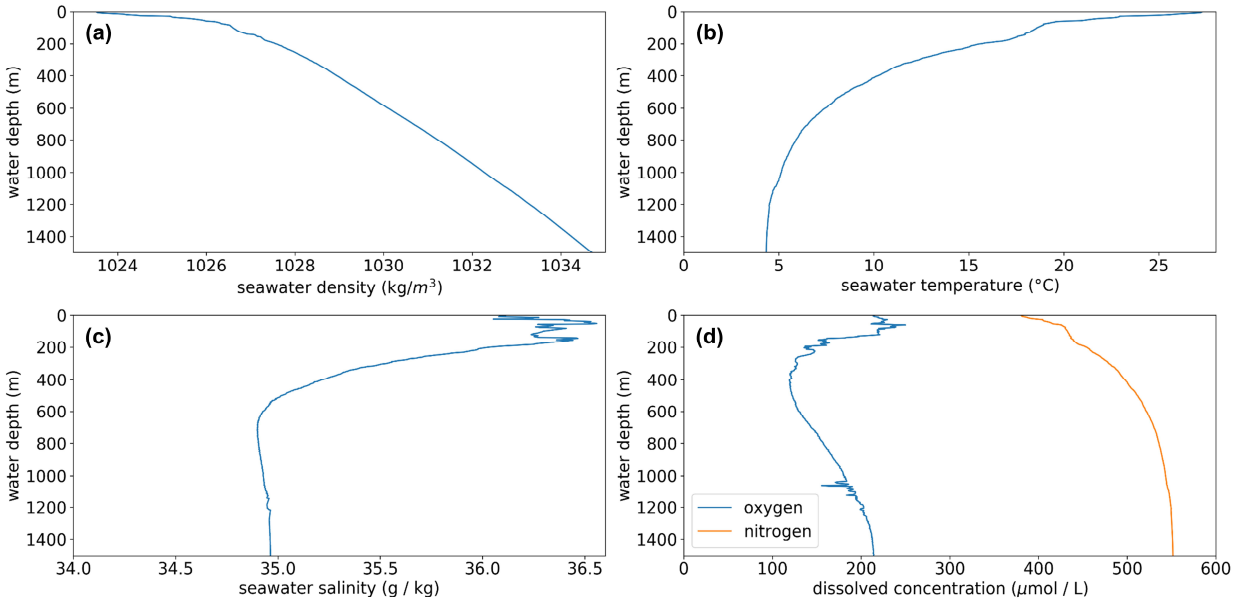

Figure S3. Measured and assumed profiles of seawater properties in the Gulf of Mexico (based on data collected at station B54 from the R/V Brooks McCall on May 30, 2010 at 28.73° N and 88.38° W). These profiles were used for the simulations of LSC live oil droplets and gas bubbles at varying water depths (Figure 5). (a) Seawater density as calculated from water depth and measured profiles of salinity and temperature, (b) seawater temperature, (c) seawater salinity, (d) aqueous concentrations of dissolved gases including oxygen (measured) and nitrogen (calculated as explained in the text). The ambient concentrations of other minor gases (e.g., argon, carbon dioxide, methane, ethane, propane) were all assumed to be 0 µmol L^{-1} for the purpose of mass transfer modeling (equation S1).

S4 Identification of phases acting as dominant limitation to mass transfer for gas-seawater; oil-seawater; gas-oil; and gas-oil-seawater interfaces

In this section, we provide the derivation of the equations describing the mass transfer across a curved two-phase interface (described as a two-boundary layer bottleneck), as well as the equations describing mass transfer across a curved three-phase interface (described as a three-boundary layer bottleneck). We then apply these equations to the four cases studied in this manuscript: gas-seawater; oil-seawater; gas-oil; and gas-oil-seawater mass transfer. For all three cases involving seawater, we show that the water-side boundary layer acts as the limiting boundary layer for methane mass transfer across these interfaces, based on boundary layer theory. These results support the following key assumptions that are employed in TAMOC simulations: (1) mass transfers from oil droplets or gas bubbles into surrounding water (i.e., aqueous dissolution) are modeled as kinetically controlled processes, due to the limitation of diffusive transport across the water side boundary layer; and (2) mass transfers between oil and gas phases are modeled as thermodynamically controlled processes (i.e., at partitioning equilibrium), owing to the comparatively swift mass transfers across the boundary layers at the oil-gas interface.

The calculations presented in this section rely on the following assumptions or approximations:

1. The interface is immobilized, i.e. “dirty” droplet or bubble (no internal circulation).
2. Gas bubbles or oil droplets are spherical objects.
3. A thin oil layer (sheen), when present, spreads uniformly over the gas-water interface of an assumed-spherical gas bubble.
4. Each phase contains a boundary layer adjacent to the interface: these boundary layers are regions where concentration gradients are observed, and they act as potential restraints on mass transfer.
5. Each boundary layer has a constant thickness.
6. The bulk phases of oil, gas, and seawater (excluding the boundary layer regions) are assumed well-mixed and thus exhibit no internal concentration gradients.

The calculations presented here are viewed as sufficient to ascertain the prominent phase driving mass transfer limitation, as the assumptions 1–6 are thought to be sufficiently close to the (more complex[20,53,54]) situation controlling mass transfer from gas bubbles and oil droplets in water. The derivation below follows the general framework outlined by Schwarzenbach et al.[13] for linear and curved interfaces.

First, we derive the equation that describes mass transfer between a 100%-gaseous bubble and seawater or a 100%-liquid droplet and seawater (Figure S4).

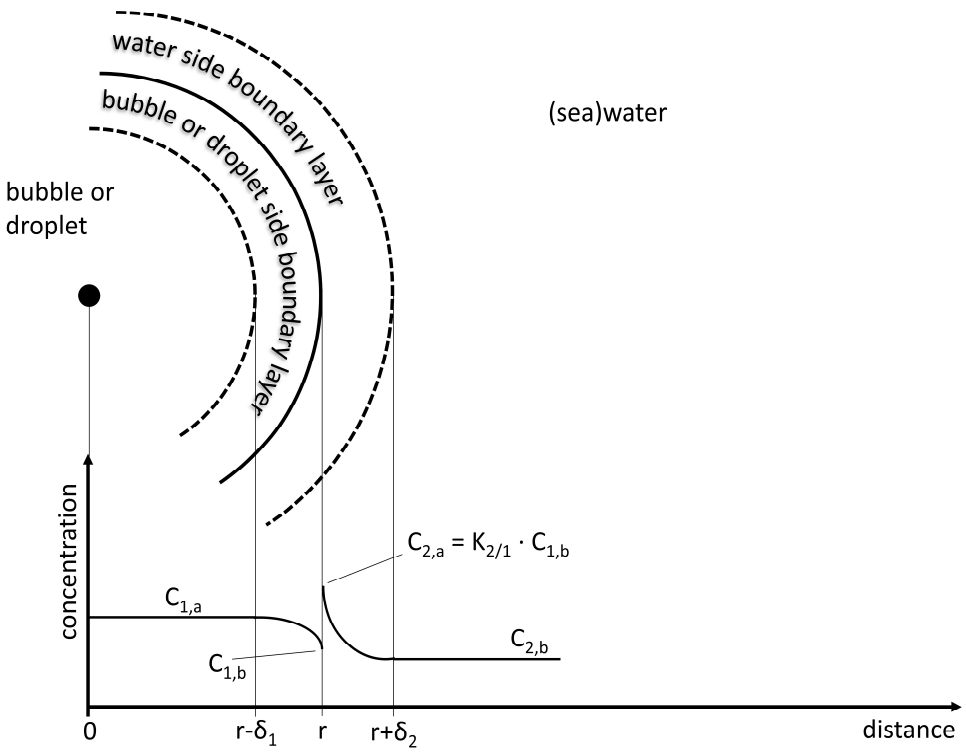

Figure S4. Schematic representation of the two boundary layers at the interface of a bubble or droplet having diameter r in (sea)water (the phase interface is shown as a solid line). The phase interface is sandwiched by two boundary layers (dashed lines) having widths of δ_1 for the gas or droplet side boundary layer and δ_2 for the water side boundary layer, respectively. Schematic concentration profiles are depicted, and the concentrations in the two phases at the interface are related through the equilibrium partition ratio $K_{2/1} = \left(\frac{C_{2,a}}{C_{1,b}}\right)_{eq}$, which is defined as the ratio of concentration in phase 2 (here seawater) at equilibrium with the concentration in phase 1 (here gas or oil). $C_{1,a}$ is the concentration in the bulk bubble or droplet phase, $C_{1,b}$ is the concentration in the bubble or droplet at the interface, $C_{2,a}$ is the concentration in the (sea)water at the interface, and $C_{2,b}$ is the concentration in the bulk of the (sea)water phase. $C_{2,b}$ is often assumed to be equal to 0 kg m^{-3} for most petroleum compounds in natural oceanic environments (section S3).

Assuming that mass transfer across the boundary is at pseudo-steady state, we can write:

$$\Sigma F_1 = \Sigma F_2 \quad \text{(S9)}$$

where index 1 represents the bubble or droplet phase, index 2 represents the seawater phase, and ΣF is the mass flow rate (mass time^{-1}), which is given by the mass flux (mass length^{-2} time^{-1}) integrated over the entire spherical phase interfacial area, and which is constant throughout each boundary layer.

The mass flow rate over the phase *i* boundary layer is given by:[13]

$$\Sigma F_i = -4\pi r^2 D_i \frac{\partial C}{\partial r} \quad \text{(S10)}$$

where D_i is the diffusion coefficient (length^2 time^{-1}) in phase *i*, *C* is the concentration (mass length^{-3}) within the boundary layer of phase *i*, and *r* is the radial distance.

Consequently:

$$\Delta C_i = \int \frac{\partial C}{\partial r} dr = \int -\frac{\Sigma F_i}{4\pi r^2 D_i} dr = -\frac{\Sigma F_i}{4\pi D_i} \cdot \int \frac{1}{r^2} dr \quad \text{(S11)}$$

where ΔC_i is the concentration difference (mass length^{-3}) across the boundary layer of phase *i*.

When applied across the two boundary layers of the interface, eq. S11 leads to:

$$\Delta C_1 = \left(C_{1,b} - C_{1,a}\right) = -\frac{\Sigma F_1}{4\pi D_1} \cdot \int_{r-\delta_1}^{r} \frac{1}{r^2} dr = -\frac{\Sigma F_1}{4\pi D_1} \cdot \left(\frac{1}{r-\delta_1} - \frac{1}{r}\right) \quad \text{(S12)}$$

$$\Delta C_2 = \left(C_{2,b} - C_{2,a}\right) = \left(C_{2,b} - K_{2/1} \cdot C_{1,b}\right) = -\frac{\Sigma F_2}{4\pi D_2} \cdot \int_{r}^{r+\delta_2} \frac{1}{r^2} dr = -\frac{\Sigma F_2}{4\pi D_2} \cdot \left(\frac{1}{r} - \frac{1}{r+\delta_2}\right) \quad \text{(S13)}$$

where δ_1 and δ_2 are the thicknesses of the boundary layers in phases 1 and 2, respectively; $K_{2/1}$ is the equilibrium partition ratio between phase 2 and phase 1 in units of (mol m^{-3}) (mol m^{-3})$^{-1}$; and the different concentration terms are as defined in Figure S4.

Eqs. S9, S12, and S13 lead to:

$$-\left(C_{2,b} - K_{2/1} \cdot C_{1,b}\right) \cdot 4\pi D_2 \cdot \frac{1}{\left(\frac{1}{r} - \frac{1}{r+\delta_2}\right)} = -\left(C_{1,b} - C_{1,a}\right) \cdot 4\pi D_1 \cdot \frac{1}{\left(\frac{1}{r-\delta_1} - \frac{1}{r}\right)} \quad \text{(S14)}$$

which can be written as:

$$C_{1,b} = \frac{C_{2,b} \cdot D_2 \cdot \frac{1}{\left(\frac{1}{r} - \frac{1}{r+\delta_2}\right)} + C_{1,a} \cdot D_1 \cdot \frac{1}{\left(\frac{1}{r-\delta_1} - \frac{1}{r}\right)}}{K_{2/1} \cdot D_2 \cdot \frac{1}{\left(\frac{1}{r} - \frac{1}{r+\delta_2}\right)} + D_1 \cdot \frac{1}{\left(\frac{1}{r-\delta_1} - \frac{1}{r}\right)}} \quad \text{(S15)}$$

Combining eqs. S13 and S15, we get:

$$\Sigma F = -4\pi \cdot \frac{D_1 \cdot \eta_1 \cdot D_2 \cdot \eta_2}{K_{2/1} \cdot D_2 \cdot \eta_2 + D_1 \cdot \eta_1} \cdot \left(C_{2,b} - C_{1,a} \cdot K_{2/1}\right) \quad \text{(S16)}$$

where $\eta_1 = \frac{1}{\left(\frac{1}{r-\delta_1} - \frac{1}{r}\right)}$, and $\eta_2 = \frac{1}{\left(\frac{1}{r} - \frac{1}{r+\delta_2}\right)}$.

Eq. S16 can be rewritten so as to introduce the overall mass transfer velocity (or mass transfer coefficient) v_{tot} (m s^{-1}):

$$v_{tot} = \frac{1}{r^2}\left(\frac{D_1 \cdot \eta_1 \cdot D_2 \cdot \eta_2}{K_{2/1} \cdot D_2 \cdot \eta_2 + D_1 \cdot \eta_1}\right) \quad \text{(S17)}$$

$$\Sigma F = -4\pi r^2 \cdot v_{tot} \cdot \left(C_{2,b} - C_{1,a} \cdot K_{2/1}\right) \quad \text{(S18)}$$

When either $K_{2/1} \cdot D_2 \cdot \eta_2 \gg D_1 \cdot \eta_1$ or $K_{2/1} \cdot D_2 \cdot \eta_2 \ll D_1 \cdot \eta_1$, only one of the two layers acts as limiting to mass transfer, and the equation S17 simplifies to:

$$v_{tot} = v_1 = \frac{1}{r^2}\left(\frac{D_1 \cdot \eta_1}{K_{2/1}}\right) = \frac{D_1}{K_{2/1}}\left(\frac{1}{\delta_1} - \frac{1}{r}\right) \quad \text{, when } K_{2/1} \cdot D_2 \cdot \eta_2 \gg D_1 \cdot \eta_1 \quad \text{(S19)}$$

$$v_{tot} = v_2 = \frac{1}{r^2}\left(D_2 \cdot \eta_2\right) = D_2 \cdot \left(\frac{1}{\delta_2} + \frac{1}{r}\right) \quad \text{, when } K_{2/1} \cdot D_2 \cdot \eta_2 \ll D_1 \cdot \eta_1 \quad \text{(S20)}$$

Equations similar to eqs. S17 and S18 can be derived for a three-layer bottleneck boundary, where a bubble is covered by a thin oil layer (sheen) immersed in seawater (Figure S5).

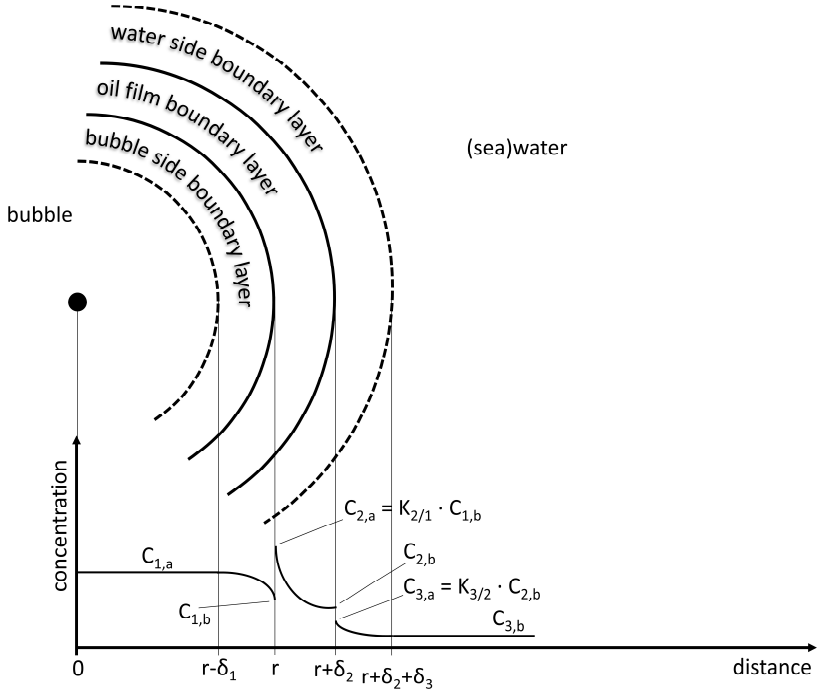

Figure S5. Schematic representation of the three boundary layers at the interfaces of a bubble having diameter r, encoated by an oil film, in a bath of surrounding (sea)water. The gas-oil interface and oil-water interface (solid lines) are sandwiched between two separate boundary layers having widths of δ_1, δ_2, and δ_3 (the gas phase, oil film, and water phase boundary layers, respectively). Schematic concentration profiles are depicted, and the concentrations at each interface are assumed to be related through the equilibrium partition ratios $K_{2/1} = \left(\frac{C_{2,a}}{C_{1,b}}\right)_{eq}$ and $K_{3/2} = \left(\frac{C_{3,a}}{C_{2,b}}\right)_{eq}$, where 1, 2, and 3 denote the gas, oil, and seawater, respectively. $C_{1,a}$ is the concentration in the bulk bubble phase, $C_{1,b}$ is the concentration in the bubble at the gas–oil interface, $C_{2,a}$ is the concentration in the oil film at the gas–oil interface, and $C_{2,b}$ is the concentration in the oil film at the oil–(sea)water interface, $C_{3,a}$ is the concentration in the (sea)water at the oil–(sea)water interface, and $C_{3,b}$ is the concentration in the bulk of the (sea)water phase.

For the sake of brevity, we do not provide the detailed derivation. Following a similar approach to eqs S9–S18 above, we obtain:

$$v_{tot} = \frac{1}{(r+\delta_2)^2}\left(\frac{D_1 \cdot \eta_1 \cdot D_2 \cdot \eta_2 \cdot D_3 \cdot \eta_3}{D_1 \cdot \eta_1 \cdot D_2 \cdot \eta_2 + D_1 \cdot \eta_1 \cdot D_3 \cdot \eta_3 \cdot K_{3/2} + D_2 \cdot \eta_2 \cdot D_3 \cdot \eta_3 \cdot K_{2/1} \cdot K_{3/2}}\right) \quad \text{(S21)}$$

where $\eta_1 = \frac{1}{\left(\frac{1}{r-\delta_1} - \frac{1}{r}\right)}$, $\eta_2 = \frac{1}{\left(\frac{1}{r} - \frac{1}{r+\delta_2}\right)}$, and $\eta_3 = \frac{1}{\left(\frac{1}{r+\delta_2} - \frac{1}{r+\delta_2+\delta_3}\right)}$.

and:

$$\Sigma F = -4\pi(r+\delta_2)^2 \cdot v_{tot} \cdot \left(C_{3,b} - C_{1,a} \cdot K_{2/1} \cdot K_{3/2}\right) \quad \text{(S22)}$$

In the analysis provided below, eqs. S17–S22 are applied to conditions relevant to both the Pesch et al.[1,55] laboratory experiments and field conditions (Tables S2, S3, S4, and S5). These expressions are used to identify the boundary layer(s) that limit mass transfer processes occurring in oil droplets, gas bubbles, two-phase droplet-bubble pairs, and gas bubbles coated with oil films.

Before discussing the results of boundary layer model calculations (further below), a brief discussion is needed on the choice of parameter values provided in Tables S2–S5, which include laboratory measurements and modeled values. The diffusion coefficient for methane in water at 50 bar was recently measured and reported in Oldenburg et al. (2020).[56] The value for methane diffusion coefficient in water by Oldenburg et al. (2020)[56] is three times greater than the value predicted by the Hayduk–Laudie formula[26] at 293.15 K, 1.01325 bar, and a salinity of 0 g kg^{-1}. The Hayduk–Laudie formula is broadly accepted[13] and well-validated for methane and a wide range of molecules.[26] Hayduk and Laudie[26] validated their formula for the diffusivities of 87 molecules in water at 298.15 K and 1.01325 bar including methane, other similar small molecules, and larger molecules. Hayduk and Laudie[26] reported a mean error of 0.3%, a mean absolute error of 5.9%, and a maximum error of 24.9% (for pentane).[26] These authors have additionally shown that their equation performs similarly to or better than four other estimation methods (Wilke–Chang, Scheibel, Othmer–Thakar, and a modified version of Wilke-Chang). We have therefore opted to use the value predicted by the Hayduk–Laudie formula here ($0.95 \cdot 10^{-9}$ m^2/s at 277.48 K, 1.01325 bar, and a salinity of 0 g kg^{-1}) as it is more consistent with pre-existing laboratory measurements at atmospheric pressure by Whiterspoon and Bonoli (1969).[57] These latter authors reported an experimental value of the diffusion coefficient of methane in water of $0.85 \pm 0.02 \cdot 10^{-9}$ m^2/s at 277.15 K, 1.01325 bar, and a salinity of 0 g kg^{-1}. The Hayduk–Laudie formula agrees with the four experimental values reported by these authors for methane at 4–60°C (spanning $0.85–3.55 \cdot 10^{-9}$ m^2/s) with an average deviation of 6.6%. The effect of pressure on diffusivities in water is poorly characterized,[30] but pre-existing experimental evidences for methane indicate that a 3-fold increase in methane diffusion coefficient at 50 bar relative to atmospheric pressure (1.01325 bar) is unlikely. For example, experimental diffusion coefficients for methane in water at 298 K and 50–400 bar have been reported in the range $1.60–1.64 \cdot 10^{-9}$ m^2/s,[58] close to another value of $1.40 \cdot 10^{-9}$ m^2/s at 82 bar,[59] and similar to the value predicted by the Hayduk–Laudie formula ($1.78 \cdot 10^{-9}$ m^2/s at 277.48 K, 1.01325 bar, and a salinity of 0 g kg^{-1}, and $1.72 \cdot 10^{-9}$ m^2/s at 277.48 K, 50 bar, and a salinity of 0 g kg^{-1}). Finally, we confirmed that choosing either the numerical value of the methane diffusion coefficient in water selected here or the value reported by Oldenburg et al. (2020)[56] both lead to the same main conclusion for the current section (mass transfer limited by the water-side boundary layer).

Table S2. Selected property values and parameters for a two-boundary layer bottleneck model (eqs. S17–S20) describing mass transfer of methane at the interface between a 100%-gaseous bubble and seawater.[a]

variable	value	rationale
$K_{2/1}$	0.016 (mol m^{-3}) (mol m^{-3})$^{-1}$	seawater-gas equilibrium ratio for methane calculated with the thermodynamic model[3] implemented in TAMOC at 277.48 K, 153 bar, and a salinity of 35 g kg^{-1} based on the composition described in section S3[b]
D_1	$100 \cdot 10^{-9}$ m^2 s^{-1}	self-diffusion coefficient of methane in super-critical phase at 297 K and 150 bar[60]
D_2	$0.95 \cdot 10^{-9}$ m^2 s^{-1}	diffusion coefficient of methane in seawater calculated with the Hayduk–Laudie[26] formula (eq. S6) at 277.48 K, 1.01325 bar, assuming a salinity of 0 g kg^{-1}
δ_1	$3 \cdot 10^{-3}$ m	boundary layer thickness suggested for a quiescent gas phase[13]
δ_2	$2 \cdot 10^{-4}$ m	boundary layer thickness suggested for a quiescent water phase[13]

[a] 1 refers to the gas phase and 2 refers to the seawater phase.

[b] a gas-liquid equilibrium calculation of the gas and oil was first performed (flash calculation) at the selected temperature and pressure. Thereafter, a gas-seawater equilibrium partitioning was performed and the corresponding methane partition ratio was calculated.

Table S3. Selected property values and parameters for a two-boundary layer bottleneck model (eqs. S17–S20) describing mass transfer of methane at the interface between a 100%-liquid droplet and seawater.[a]

variable	value	rationale
$K_{2/1}$	0.032 (mol m^{-3}) (mol m^{-3})$^{-1}$	seawater-oil equilibrium ratio for methane calculated with the thermodynamic model[3] implemented in TAMOC at 277.48 K, 153 bar, and a salinity of 35 g kg^{-1} based on the composition described in section S3[b]
D_1	$1 \cdot 10^{-9}$ m^2 s^{-1}	diffusion coefficient of methane in Louisiana Sweet crude oil at 50 bar[56]
D_2	$0.95 \cdot 10^{-9}$ m^2 s^{-1}	diffusion coefficient of methane in seawater calculated with the Hayduk–Laudie[26] formula (eq. S6) at 277.48 K, 1.01325 bar, assuming a salinity of 0 g kg^{-1}
δ_1	$2 \cdot 10^{-4}$ m	boundary layer thickness suggested for a live oil phase, assumed similar to the value used for a quiescent water phase,[13] owing to the similarity in estimated viscosities of these two fluids at *Deepwater Horizon* deep-sea conditions[2]
δ_2	$2 \cdot 10^{-4}$ m	boundary layer thickness suggested for a quiescent water phase[13]

[a] 1 refers to the oil phase and 2 refers to the seawater phase.

[b] a gas-liquid equilibrium calculation of the gas and oil was first performed (flash calculation) at the selected temperature and pressure. Thereafter, an oil-seawater equilibrium partitioning calculation was performed and the corresponding methane partition ratio was determined.

Table S4. Selected property values and parameters for a three-boundary-layer bottleneck model (eqs. S21 and S22) describing mass transfer of methane from a gas bubble, through a thin oil film, and into seawater.[a]

variable	value	rationale
$K_{2/1}$	0.50 (mol m^{-3}) (mol m^{-3})$^{-1}$	oil-gas equilibrium ratio for methane calculated with the thermodynamic model[3] implemented in TAMOC at 277.48 K, and 153 bar, based on the composition described in section S3[b]
$K_{3/2}$	0.032 (mol m^{-3}) (mol m^{-3})$^{-1}$	seawater-oil equilibrium ratio for methane calculated with the thermodynamic model[3] implemented in TAMOC at 277.48 K, 153 bar, and a salinity of 35 g kg^{-1} based on the composition described in section S3[c]
D_1	$100 \cdot 10^{-9}$ m^2 s^{-1}	self-diffusion coefficient of methane at 297 K and 150 bar[60]
D_2	$1 \cdot 10^{-9}$ m^2 s^{-1}	diffusion coefficient of methane in Louisiana Sweet crude oil at 50 bar[56]
D_3	$0.95 \cdot 10^{-9}$ m^2 s^{-1}	diffusion coefficient of methane in seawater calculated with the Hayduk–Laudie[26] formula (eq. S6) at 277.48 K, 1.01325 bar, assuming a salinity of 0 g kg^{-1}
δ_1	$3 \cdot 10^{-3}$ m	boundary layer thickness suggested for a quiescent gas phase[13]
δ_2	$3 \cdot 10^{-7}$–$2 \cdot 10^{-4}$ m	typical oil sheen thickness (corresponding to "bright colors" for a sheen on the sea surface)[61] – assumed maximum oil layer thickness (corresponding to the boundary layer thickness selected in Table S3)
δ_3	$2 \cdot 10^{-4}$ m	boundary layer thickness suggested for a quiescent water phase[13]

[a] 1 refers to the gas phase, 2 refers to the oil phase, and 3 refers to the seawater phase.

[b] a gas-liquid equilibrium calculation of the gas and oil was performed (flash calculation) at the selected temperature and pressure, and the corresponding methane partition ratio was determined.

[c] a gas-liquid equilibrium calculation of the gas and oil was first performed (flash calculation) at the selected temperature and pressure. Thereafter, an oil-seawater equilibrium partitioning calculation was performed and the corresponding methane partition ratio was determined.

Table S5. Selected property values and parameters for a two-boundary layer bottleneck model (eqs. S17–S20) describing mass transfer of methane at the interface between a 100%-gaseous bubble and live oil.[a]

variable	value	rationale
$K_{2/1}$	0.50 (mol m^{-3}) (mol m^{-3})$^{-1}$	oil-gas equilibrium ratio for methane calculated with the thermodynamic model[3] implemented in TAMOC at 277.48 K, and 153 bar, based on the composition described in section S3[b]
D_1	$100 \cdot 10^{-9}$ m^2 s^{-1}	self-diffusion coefficient of methane in super-critical phase at 297 K and 150 bar[60]
D_2	$1 \cdot 10^{-9}$ m^2 s^{-1}	diffusion coefficient of methane in Louisiana Sweet crude oil at 50 bar[56]
δ_1	$3 \cdot 10^{-3}$ m	boundary layer thickness suggested for a quiescent gas phase[13]
δ_2	$2 \cdot 10^{-4}$ m	boundary layer thickness suggested for a live oil phase, assumed similar to the value used for a quiescent water phase,[13] owing to the similarity in estimated viscosities of these two fluids at *Deepwater Horizon* deep-sea conditions[2]

[a] 1 refers to the gas phase and 2 refers to the oil phase.

[b] a gas-liquid equilibrium calculation of the gas and oil was performed (flash calculation) at the selected temperature and pressure, and the corresponding methane partition ratio was determined.

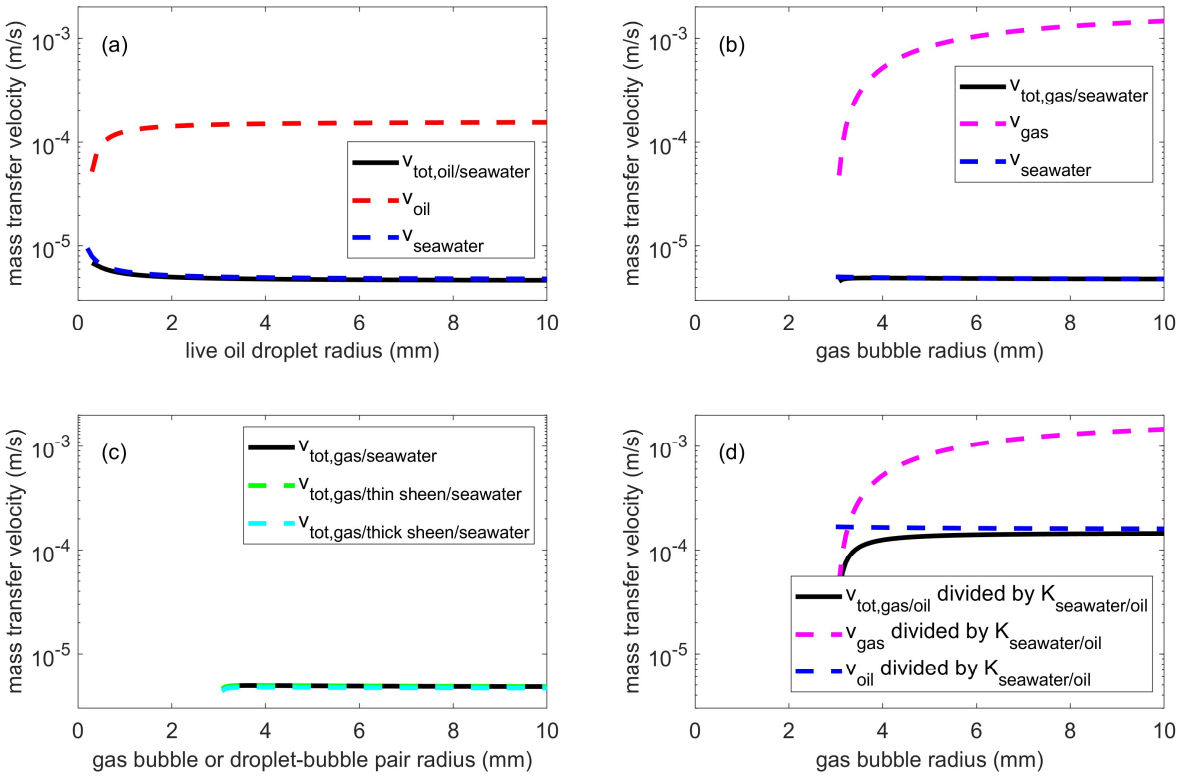

Figure S6. (a) Modeled mass transfer velocity of methane across a live oil droplet-seawater interface according to eqs. S17–S20 and assuming properties reported in Table S3. The overall mass transfer velocity, $v_{tot,oil/seawater}$ (eq. S17), is compared to the seawater-boundary layer mass transfer velocity, $v_{seawater}$ (eq. S20), and the oil boundary layer mass transfer velocity, v_{oil} (eq. S19). (b) Mass transfer velocity of methane across a bubble-seawater interface according to eqs. S17–S20 and assuming properties reported in Table S2. The overall mass transfer velocity, $v_{tot,gas/seawater}$ (eq. S17), is compared to the seawater-boundary layer mass transfer velocity, $v_{seawater}$ (eq. S20), and the gas-boundary layer mass transfer velocity, v_{gas} (eq. S19). (c) The overall mass transfer velocity of methane across a bubble-seawater interface according to eq. S17 and assuming properties reported in Table S2, $v_{tot,gas/seawater}$, is compared to the mass transfer velocity of methane across a bubble-oil film-seawater interface according to eq. S21 and assuming properties reported in Table S4. The "thin" ($3 \cdot 10^{-7}$ m) and "thick" ($2 \cdot 10^{-4}$ m) oil films represent the range of likely oil film thicknesses suggested in Table S4 and indicate that the resulting mass transfer velocity is independent of the oil film thickness over the investigated range. (d) Modeled mass transfer velocity of methane across a gas bubble-live oil interface according to eqs. S17–S20 and assuming properties reported in Table S5. The overall mass transfer velocity, $v_{tot,gas/oil}$ (eq. S17), is compared to the oil-boundary layer mass transfer velocity, v_{oil} (eq. S20), and the gas boundary layer mass transfer velocity, v_{gas} (eq. S19). On panel (d), the mass transfer velocities are divided by $K_{seawater/oil}$ to make the numerical values directly comparable to panels a–c. Because the equations are defined only for droplet or bubble diameters larger than the boundary layer thickness, calculated curves are shown only for gas bubble radius >3 mm on panels b–d.

Results from the boundary layer models support the TAMOC model assumption that the limitation to mass transfer of methane lies in the seawater boundary layer for either a gas bubble (Figure S6b, eq. S17), a live oil droplet (Figure S6a, eq. S17), or both the gas and oil phases of a droplet-bubble pair (Figure S6a–d, eqs. S17, and S21). Additionally, boundary layer calculations indicate that methane dissolution from deep-sea gas bubbles would not be slowed by the presence of a liquid oil film coating at the gas-water interface (Figure S6c), because methane dissolution from these bubbles is limited by the water side boundary layer. The finding for oil film-coated gas bubbles is unaffected by the oil layer for the investigated range of oil film thicknesses ($3 \cdot 10^{-7}$–$2 \cdot 10^{-4}$ m) spanning three orders of magnitude.

Additionally, these boundary-layer model results indicate that gas-oil transfer of methane (Figure S6d, eq. S17) is a fast process compared to aqueous dissolution of methane from either droplets or bubbles (Figure S6a–b, eq. S17 and Figure S6c, eq. S21). This outcome supports the interpretation that aqueous dissolution is a kinetically controlled process, whereas the dynamics of gas-oil partitioning, ebullition, and condensation can be approximated by the thermodynamic phase equilibria arising from the dynamical changes in pressure, temperature, and chemical composition.

S5 Supersaturation by aqueously-dissolved gases and ebullition of the vessel seawater near the end of the live oil experiments of Pesch et al.[1]

For all experiments involving live oil droplets by Pesch et al.[1] (experiments 1–9), TAMOC simulations confirm that aqueously-dissolved gases became supersaturated during the low pressures (1–1.5 bar) encountered by the vessel during the final seconds to minutes of the experiments (gray-shaded regions in Figures 2a, 3a, and S8a), which enabled the thermodynamically-spontaneous formation of gas bubbles from the water phase. This would explain the reportedly-observed formation of gas bubbles throughout the water phase during the final time points of experiment 2 (visibly apparent in the right-most panel of Figure 1b). The TAMOC model does not explicitly simulate ebullition of aqueously-dissolved gas from the water phase, and this process typically would not be relevant in the natural environment. Rather, ebullition of dissolved gases from water resulted from a particular sequence of conditions that were unique to the Pesch et al.[1] experiments: prior to the onset of each experiment, the vessel water was initially equilibrated with atmospheric gases at 1 atm. Consistent with these initial conditions of the experiment, TAMOC simulations assume that the initial concentrations of N_2 and O_2 in the seawater (at the onset of the experiment) were determined by equilibrium with respect to atmospheric gases at 1 atm. When used to describe the course of the experiments, TAMOC simulations predict that significant quantities (97–99.8%) of the available methane in the live oil droplet became dissolved in the vessel water, because the aqueous equilibrium concentration of methane became greatly increased by the high pressure conditions of the laboratory vessel during the experiments. However, near the end of each experiment, when the pressure of the vessel approached near-atmospheric values (<1.5 bar), the water became supersaturated by these dissolved gases (i.e., the sum of fugacities of methane, N_2, and O_2 exceeded the pressure in the vessel). This apparently resulted in the formation of a gas phase directly from seawater, analogous to the commonly observed ebullition of dissolved gases that occurs when a pressurized bottle of carbonated beverage is opened at ambient atmospheric pressure. In the experiment of Pesch et al.,[1] the ebullition of gases from the water phase was facilitated by the presence of the dissolved atmospheric gases that were initially present in the water, and therefore the resulting gas bubbles necessarily contained a mixture of methane, N_2, and O_2. In the absence of these dissolved atmospheric gases that were innocuously introduced prior to the experiment, the build-up of aqueously dissolved methane during experiments 4–9 would have been insufficient to cause thermodynamically-spontaneous ebullition of gas from either the water phase or the oil droplet. In summary, the ebullition of gas bubbles from the water phase is a particular outcome related to the confined water volume and laboratory setup of the experiments of Pesch et al.;[1] and we would not expect ebullition from the water phase to happen during the typical conditions of a live oil release in the environment.

S6 Predicted situation during the laboratory experiments 1–3 of Pesch et al.[1] with suppressed aqueous dissolution

To further illustrate the important role of aqueous dissolution, Figure S7 presents TAMOC predictions of the situation during the experiments 1–3 of Pesch et al.,[1] but with aqueous dissolution disabled in the model. This corresponds to the assumption made by Pesch et al.[1] in the calculations they conducted to interpret the situation prevailing during deep-water oil spills.[1] As indicated by Figure S7, this assumption is not consistent with the experimental observations of Pesch et al.[1] To the contrary, enabling aqueous dissolution in TAMOC leads to good agreement between predicted and observed droplet diameters, whereas neglect of aqueous dissolution produces unreasonably large deviations between predicted and observed values (Figure 2a, Table 1). Figure S7 further illustrates that the simulated bubble point pressure curve, methane apportionments, gas and liquid volume fractions, and fluid densities follow trajectories that differ substantially from the simulated quantities shown in Figure 2. In summary, TAMOC predictions would fail to explain the laboratory experiments 1–3 of Pesch et al.[1] unless aqueous dissolution is included in the model. This and other evidence lead us to conclude that aqueous dissolution is the dominant control on methane behavior both during the laboratory experiments of Pesch et al.[1] and also during the *Deepwater Horizon* disaster (further discussed in the main text).

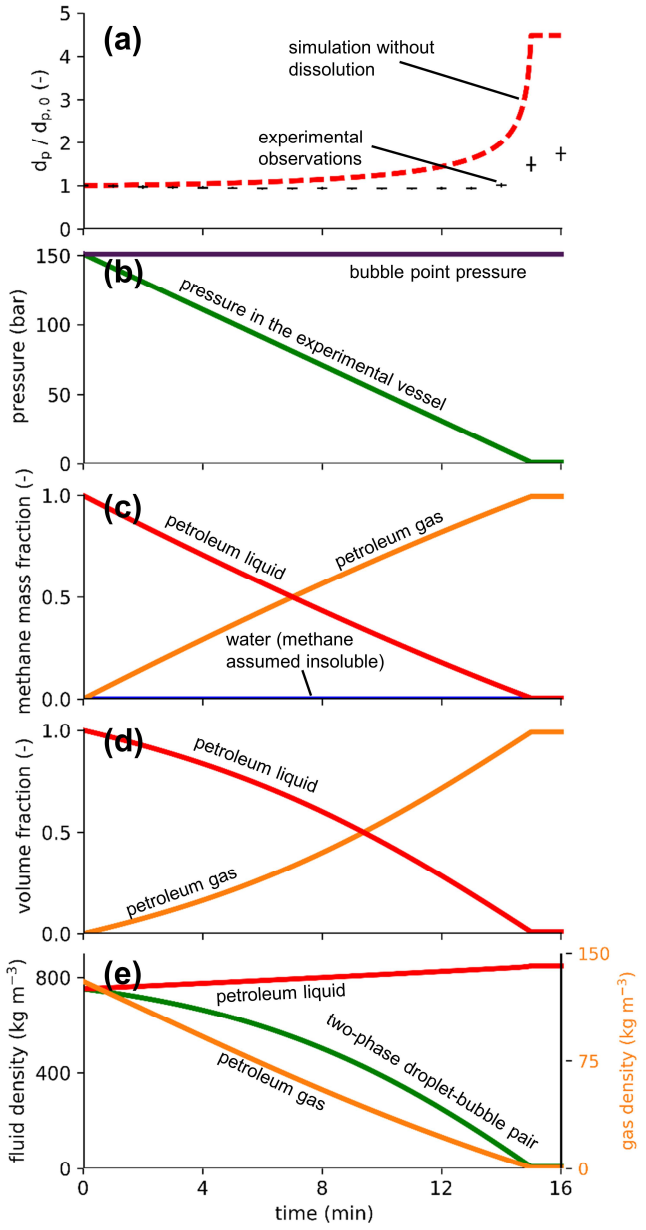

Figure S7. TAMOC simulation of the situation during the laboratory experiments 1–3 of Pesch et al.[1] if aqueous dissolution of methane would not have happened. This simulation shows substantial disagreement with laboratory observations (panel a), illustrating the importance of aqueous dissolution of methane during a release of live oil in deep water (Figure 2a in main text). (a) Relative diameter of oil droplets in experiments 1–3: TAMOC simulations with aqueous dissolution suppressed (red dashed line) are compared to laboratory observations of Pesch et al.[1,55] (black crosses: the horizontal line displays the arithmetic average; the vertical line indicates the measured range spanned by 3 experiments). (b) Absolute pressure within the experimental vessel (green line, decompression rate of 10 bar min^{-1}) and simulated bubble point pressure at the experimental temperature of 20°C (purple line). (c) Modeled mass fractions of total methane in the experimental vessel: dissolved in seawater (blue line), dissolved in oil liquid (red line), and gaseous (orange line). (d) Modeled fractions of total volume of the droplet-bubble pair represented by oil liquid (red line) and gas (orange line). (e) Modeled oil density (red line, left axis), aggregate density of the two-phase droplet-bubble pair (green line, left axis), and gas-phase density (orange line, right axis).

S7 TAMOC simulation of experiments 4–6 by Pesch et al.[1]

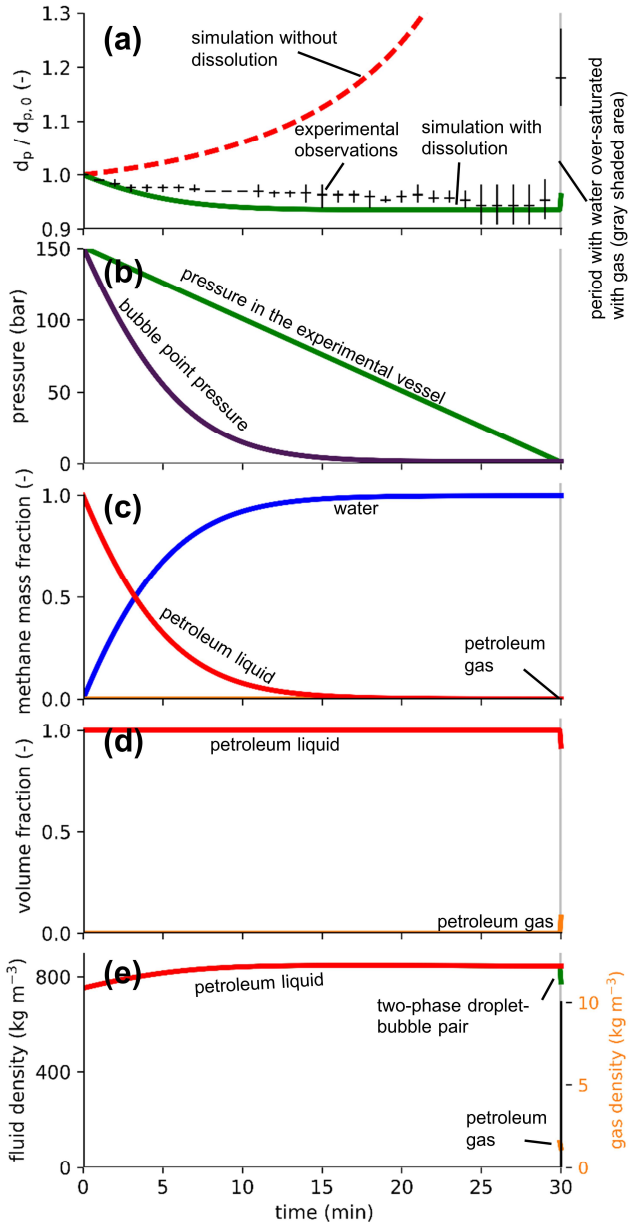

Figure S8. (a) Relative diameter of oil droplets in experiments 4–6: TAMOC simulations (solid green line) are compared to laboratory observations of Pesch et al.[1,55] (black crosses: the horizontal line displays the arithmetic average; the vertical line indicates the measured range spanned by 3 experiments). Also shown are results of TAMOC simulations with aqueous dissolution suppressed (red dashed line). (b) Absolute pressure within the experimental vessel (green line, decompression rate of 5 bar min^{-1}) and simulated bubble point pressure at the experimental temperature of 20°C (purple line). (c) Modeled mass fractions of total methane in the experimental vessel: dissolved in seawater (blue line), dissolved in oil liquid (red line), and gaseous (orange line). (d) Modeled fractions of total volume of the droplet-bubble pair represented by oil liquid (red line) and gas (orange line). (e) Modeled oil density (red line, left axis), aggregate density of the two-phase droplet-bubble pair (green line, left axis), and gas-phase density (orange line, right axis). The gray-shaded area (final 3 s of the experiment) indicates the period during which the vessel water was predicted to be over-saturated with gases, leading to thermodynamically-spontaneous formation of a gas phase from water (this phase transition was not simulated).

S8 TAMOC simulation of experiments 10–12 by Pesch et al.[1]

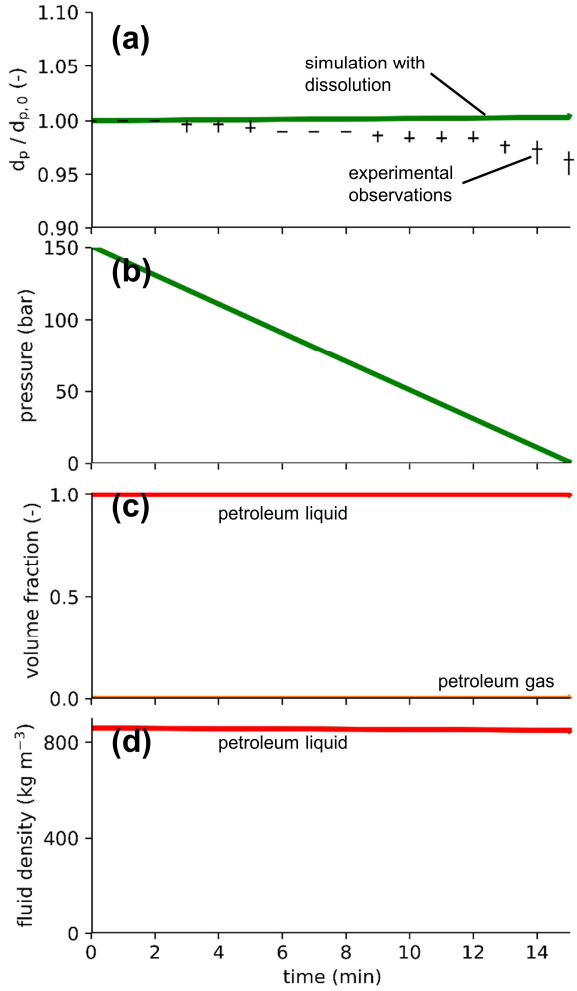

Figure S9. (a) Relative diameter of dead oil droplets in experiments 10–12: TAMOC simulations (solid green line) are compared to laboratory observations of Pesch et al.[1,55] (black crosses: the horizontal line displays the arithmetic average; the vertical line indicates the measured range spanned by 3 experiments). (b) Absolute pressure (decompression rate of 10 bar min^{-1}). (c) Modeled fraction of total volume of the oil droplet represented by oil liquid (red line) and gas (orange line). (d) Modeled oil density (red line).

S9 Predicted slip velocities of methane-free and methane-saturated oil droplets as a function of droplet diameter

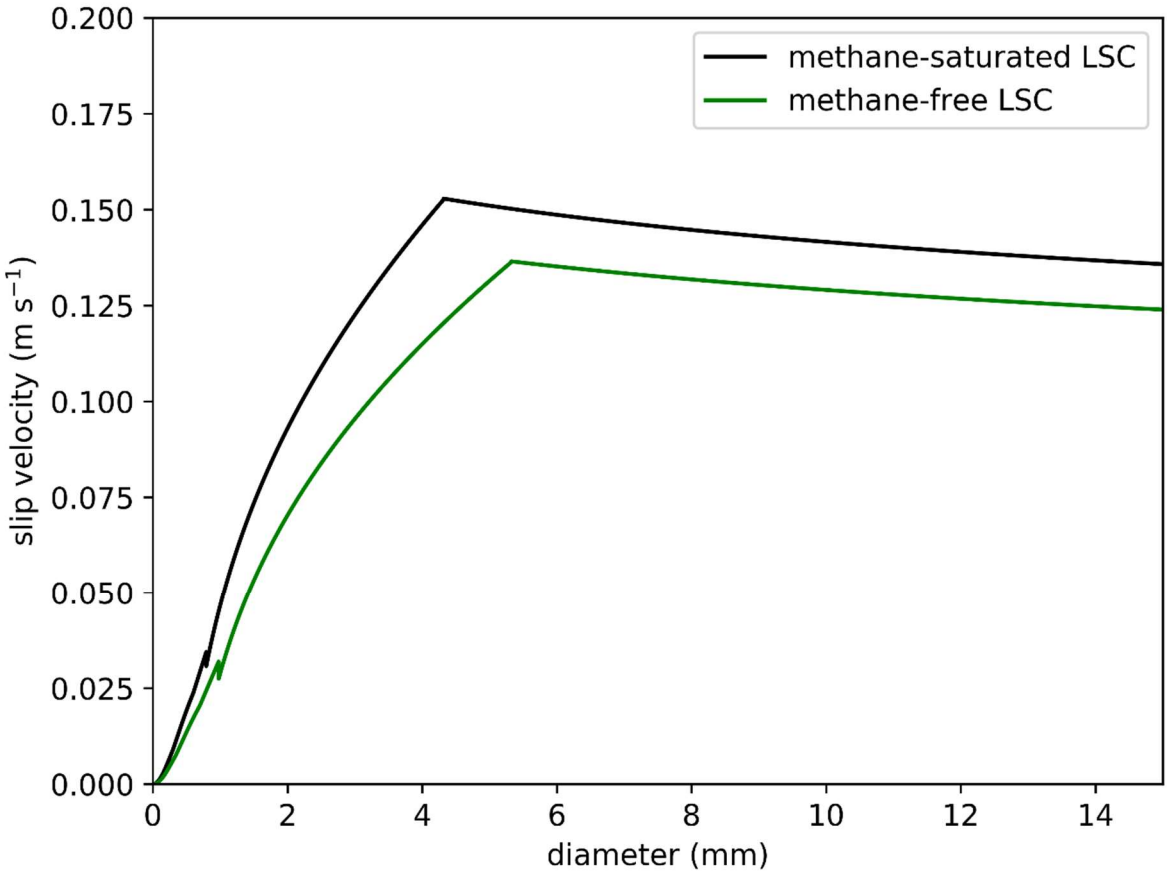

Figure S10. Slip velocities (vertical velocities relative to ambient seawater) predicted with TAMOC[2,4] (calculated according to the method of Clift et al.[20], section S1) for methane-saturated and methane-free LSC oil at 151 bar, 20°C, and a salinity of 35 g kg^{-1}.

S10 Predicted vertical velocity of the multiphase buoyant plume during the 2010 *Deepwater Horizon* disaster

During the 2010 *Deepwater Horizon* disaster, the positively buoyant oil and gas fluids emitted at ~1500 m water depth initiated a buoyant plume constituted of entrained seawater, oil droplets, and gas bubbles.[62] At ~1100 m depth, the buoyancy brought by the dispersed droplets and bubbles became insufficient to further lift the entrained seawater,[2,62] and an intrusion layer formed[2,62–64] constituted of the former plume seawater, aqueously dissolved petroleum compounds (by mass, >90% C_1–C_5 and CO_2, with the remainder chiefly constituted of BTEX compounds),[2,37,65,66] and microdroplets having insufficient buoyancy to rapidly escape the intrusion.[2,67,68] It has been postulated that, above the intrusion layer, droplets and bubbles would be sufficiently spread out to ascend farther without formation of subsequent plume structure(s).[2,42,69,70] The multiphase plume model in TAMOC was previously validated with laboratory and

field-scale data for single-phase and multiphase plumes. Laboratory validation studies include 11 different datasets for single-phase plumes in diverse conditions, 4 bubbly jets, 17 bubble plumes in quiescent conditions, 13 bubble plumes in stratified stagnant conditions, and 30 bubble plumes in cross flowing conditions, including stratified crossflow.[4] At the field scale, TAMOC was validated to plume trajectories and trap height data from the *DeepSpill* experiment[4] and dissolved concentration data within the deep-water hydrocarbon-rich intrusion and concentrations of hydrocarbons released to the atmosphere from the sea surface during *Deepwater Horizon* disaster.[2]

The predicted instantaneous vertical velocity of the buoyant plume on June 8, 2010 is shown in Figure S11 (see section S2 and previous work[2] for a complete description of simulation assumptions). According to these simulations, the average vertical plume velocity on June 8, 2010 was 0.36 m s^{-1}, for depths spanning 1505 m (Macondo wellhead) to 1100 m (intrusion depth). By comparison, the high ascent velocities corresponding to the decompression rates of experiments 1–6 of Pesch et al.[1] are predicted to have happened only within the first few meters above the emission source on June 8, 2010 during the *Deepwater Horizon* disaster.

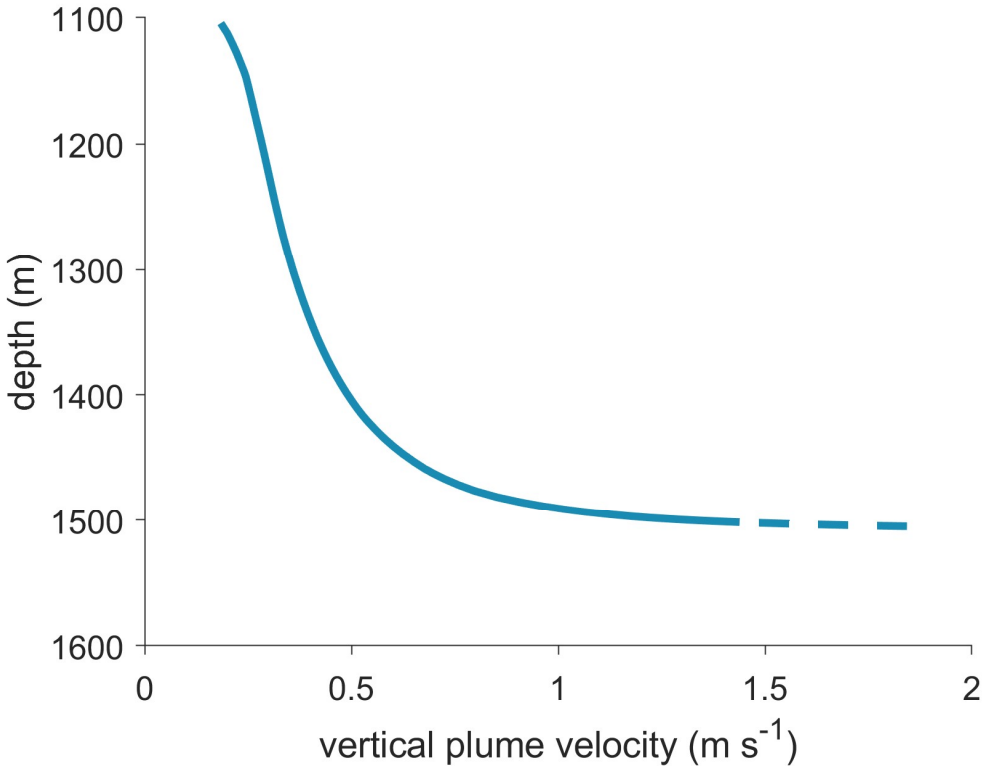

Figure S11. Predicted instantaneous vertical plume (seawater) velocity between the pared Macondo wellhead (1505 m water depth) and the deep-water hydrocarbon-rich intrusion at 1100 m water depth, on June 8, 2010. These velocities are for a "top-hat" velocity profile (single velocity value over the plume representative of the average plume behavior). Real plumes have Gaussian velocity profiles, which can be calculated from top-hat velocities through known equations.[71] The dashed line corresponds to the estimated value within the zone of flow establishment (defined as the region from the wellhead to a vertical distance of 6 orifice diameters, or 3 m). The model assumptions are further described in section S2 and in a previous work.[2] In addition to vertical plume (seawater) velocity, individual droplets and bubbles have a vertical velocity component ("slip velocity") arising from their buoyancy relative to the plume seawater (Figure S10). For the depths spanned by Figure S11, the slip velocity is smaller than the vertical plume (seawater) velocity.

S11 Compared to typical deep-water conditions, experiments 1–9 of Pesch et al.[1] unrealistically favored ebullition of the live oil droplets

Compared to typical conditions of open deep water, the artificial conditions of experiments 1–9 (Figures 2, 3, and S8) unrealistically favored ebullition of the live oil droplets over aqueous dissolution for several reasons. First, the accumulation of aqueously-dissolved methane within the closed experimental vessel suppressed the methane dissolution rate (by up to 5.7%, 93%, and 100% before the ebullition of the live oil droplet during experiments 1–3, 4–6, and 7–9, respectively) and also artificially caused the supersaturation of the water phase during later time points of experiments 1–9 (at pressures <1.5 bar; further explained in section S5). Second, the decompression rates of 5 and 10 bar min^{-1} correspond to a droplet rising through the water column at a vertical velocity of 0.85–1.7 m s^{-1}, which is 5–10× faster than the rise rate that would result from buoyancy-driven ascent of isolated monophasic petroleum droplets (Figure S10)[2,35] and 1.4–3.7× greater than plume rise velocities in the multiphase *Deepwater Horizon* plume (Figure S11). The vertical velocities prevailing during experiments 1–6 correspond to conditions encountered in the initial tens of meters of buoyant plumes, but are faster than the average vertical plume velocity predicted during the *Deepwater Horizon* disaster: 0.36 m s^{-1} over 1505–1100 m depth (section S10). Finally, the 20°C temperature of the water (which averted formation of hydrates within the experimental vessel) decreased the aqueous equilibrium concentration of methane relative to typical deep-water temperatures (1–5°C[47]) that would be experienced during ascent through most of the water column. However, hydrate shells might be expected to form on live oil droplets in deep waters, which may slow down aqueous dissolution kinetics. Despite the fact that most of these conditions favor droplet ebullition over aqueous dissolution of methane, TAMOC simulations and experimental observations nonetheless both indicate that aqueous dissolution was unequivocally the dominant process that drove ≥97% of the methane out of the live petroleum droplets during experiments 1–9.

S12 Phase behaviors of single-component fluids versus multicomponent fluids

The properties of pure methane have been sometime invoked to represent the behavior of natural gas released under deep-water conditions. This has led to misunderstanding about live fluid and gas behaviors in deep water, because this single-component fluid exhibits a very different phase behavior than multicomponent fluids (e.g., natural gas or petroleum fluid) under high-pressure conditions.

The Gibbs phase rule[72] states that:

$$\mathrm{F} = C - P + 2 \tag{S23}$$

where F is the number of degrees of freedom, C is the number of components, and P is the number of phases present.

Single-component fluids. A single-component fluid is composed of a single chemical (for example, pure methane). This type of fluid has only a single equilibrium phase at a chosen pressure and temperature. From eq. S23, we see that setting C=1 and P=1 will produce F=2, which means that fixing the pressure and temperature will fully constrain the conditions of the system at thermodynamic equilibrium. The dependence of phase behavior on pressure and temperature conditions can be described by a *phase diagram*. In a single-component phase diagram (Figure S12a), lines separate the different possible phase states (solid, liquid, and gas). If a line is crossed by changing the pressure and/or temperature conditions of the system, this corresponds to an abrupt change in the phase state, assuming thermodynamic equilibrium. The gas-liquid equilibrium line ends at a point called the *critical point*. At this point (defined by a set of critical pressure, P_c, and critical temperature, T_c), the properties of the liquid and the properties of the gas converge on one another. At pressures and temperatures above the critical point, the fluid is in a *super-critical* state, where no abrupt phase transition can occur. A super-critical fluid smoothly transitions to a gas or liquid if, respectively, the pressure or the temperature is decreased below its critical value. Super-critical fluids have properties that lie in between those of gases and liquids. Phase states such as "solid", "liquid", "gaseous", and "super-critical" are adjectives that apply to phases, and not to individual chemicals.

For example, for pure methane P_c = 46 bar and T_c = 190.6 K. Consequently, a hypothetical bubble made of pure methane at water depths >450 m is a super-critical fluid, which would smoothly transition to a gas at 450 m water depth (i.e. no sharp transition will be noticed). Pure methane at 50 bar and 278 K is a super-critical fluid, which is the only equilibrium state that this chemical can have under these conditions. However, we will see in the next paragraph that multicomponent mixtures enable methane to reside simultaneously in two different phases at fixed conditions of pressure and temperature. Thus, TAMOC simulations with pure methane would not be able to represent the dual-phase states that arise for real natural gas mixtures and petroleum fluids.

Multicomponent mixtures. A multicomponent mixture has a phase diagram (often referred to as *phase envelope*, Figure S12b) that is fundamentally different from the phase diagram of a single-component fluid. The phase envelope of a multicomponent fluid contains a two-phase region where both a gas and a liquid phase coexist at thermodynamic equilibrium. The phase envelope of a multicomponent mixture (Figure 12b) contrasts markedly with the phase diagram of a single-component fluid (Figure S12a); the latter does not contain a two-phase region, due to the Gibbs phase rule. Typically, the two-phase region is bounded by a dew-point line and a bubble-point line which meet at the critical point. The dew-point line marks the transition from a pure gas to a two-phase region, whereas the bubble-point line marks the transition from a pure liquid to a two-phase region. Ebullition of a single-phase liquid corresponds to crossing the bubble-point line, whereas condensation of a single-phase gas corresponds to crossing the dew-point line. Within the two-phase region, a single chemical (e.g. methane) may be found in two different states: some of the chemical is present within the gas phase, and some of it resides in the liquid phase. For example, field observations and equation-of-state calculations indicate that petroleum fluids released at the broken wellhead during the *Deepwater Horizon* at 153 bar and 277.45 K separated into a gas and a liquid phase, which means that these conditions (pressure, temperature, composition) occupied the two-phase region of the phase envelope.[3,42,73–75] Equation-of-state calculations[3] have shown that methane would partition approximately equally between the liquid and gas phases at these conditions. Therefore, the states that arise in the phase envelope of a multicomponent fluid must not be confused with the states of pure methane (described above). At 153 bar and 277.45 K, pure methane would be a

super-critical fluid, however no one phase or substance can be “super-critical” within a multiphase system.

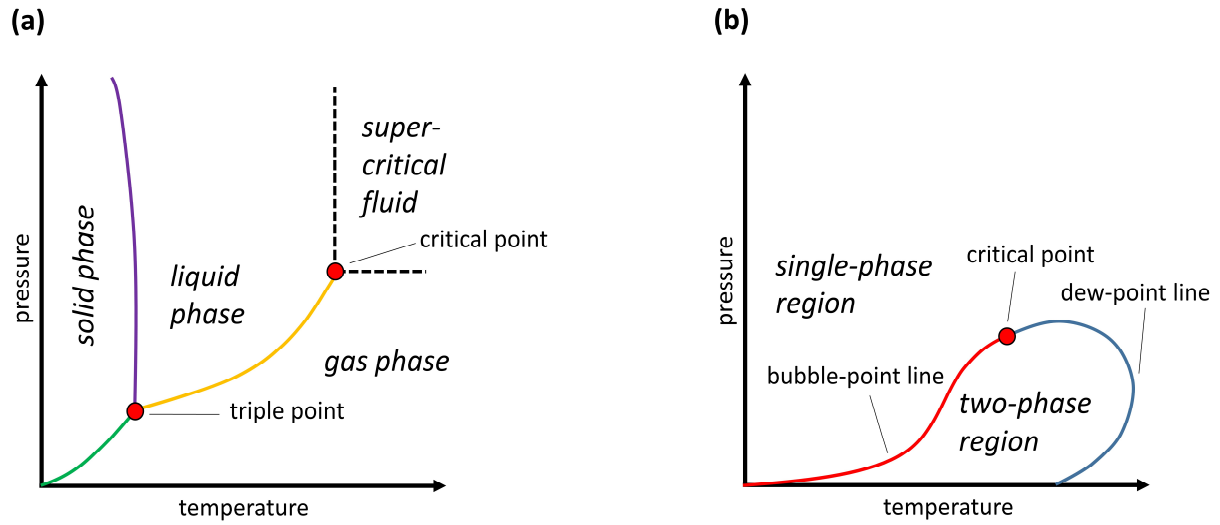

Figure S12. (a) Schematic depiction of an example phase diagram of a single-component fluid. (b) Schematic depiction of an example phase diagram of a multicomponent fluid.

The shape of the phase envelope is dependent on the composition of the multicomponent mixture. For the experiments of Pesch et al. (2018),[1] our TAMOC simulations show that the phase envelope of the oil droplet shrinks with time due to rapid loss of methane through aqueous dissolution. The simulated phase envelopes at selected time points of experiments 1–3 are shown in Figure S13. As can be seen on the figure, the phase envelope initially shrinks faster—due to the kinetically-controlled loss of methane through aqueous dissolution—than the rate at which the system pressure was decreased within the experimental vessel. Consequently, the conditions of temperature and pressure within the experimental vessel—that were on the edge of the phase envelope at the start of the experiment—moved into the single-phase region and they initially trail farther and farther behind the retracting bubble-point line. However, near the end of the experiment, the rate of shrinkage of the phase envelope decreases (due to a decreased rate of compositional change once most of the methane has already escaped the droplet). Finally, at 14.3 min in the simulations, the conditions in the experimental vessel again meet the edge of the phase envelope: the system pressure in the experimental vessel (8.1 bar) equals the bubble-point pressure of the droplet at the experimental temperature of 293.15 K. Consequently, ebullition happens at this point in time, assuming gas-liquid thermodynamic equilibrium. Thereafter, the droplet-bubble pair remained biphasic (i.e., within the limits of the phase envelope) until the end of experiments 1–3. Panels b of Figures 2, 3, and S8 depict both the bubble-point pressure (at constant temperature) and the system pressure conditions within the experimental vessel over the duration of the experiments by Pesch et al.,[1] for the three sets of experiments involving live oil. Simulations assume that the droplet remains monophasic as long as the pressure within the experimental vessel remains larger than the simulated bubble-point pressure at the experimental temperature, whereas gas formation becomes

thermodynamically spontaneous once these lines cross and the pressure within the experimental vessel becomes smaller than the simulated bubble point pressure.

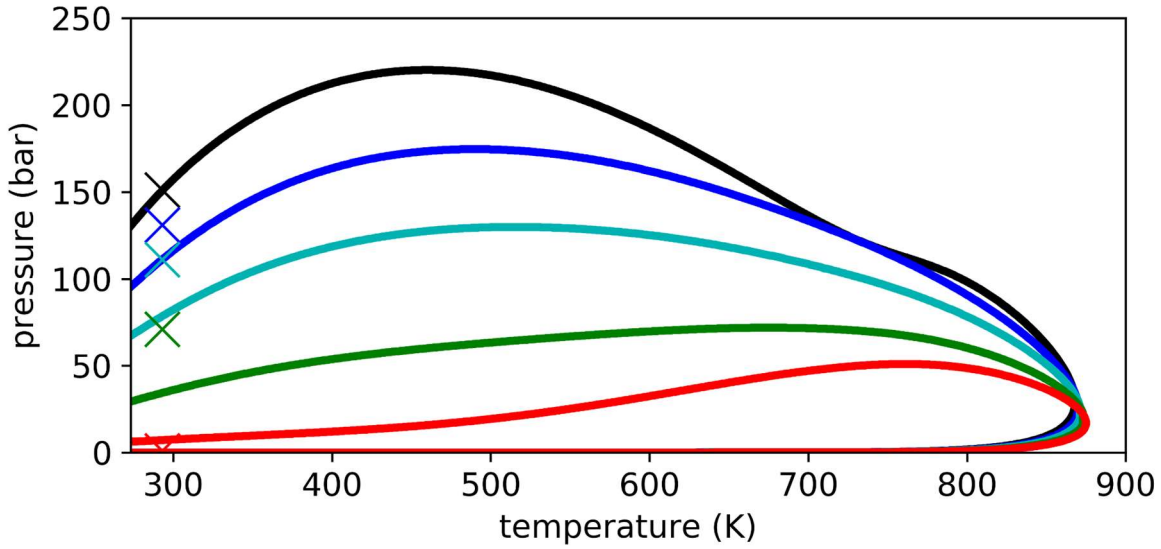

Figure S13. TAMOC-simulated phase envelopes (solid lines) and conditions of temperature and pressure within the experimental vessel (crosses) at five time points during experiments 1–3 of Pesch et al.:[1] 0 min (black), 2 min (dark blue), 4 min (turquoise), 8 min (green), and 15 min (red). At the onset of the experiment (black), the conditions within the experimental vessel lie on the edge of the phase envelope; whereas at 2, 4, and 8 min, the conditions within the experimental vessel lie outside the corresponding phase envelopes (i.e. the droplet is single phase); and finally at 15 min, the conditions within the experimental vessel lie within the corresponding phase envelope, and therefore the droplet exhibits two phases (gas and liquid) at gas-liquid thermodynamic equilibrium. Phase envelopes were calculated with the Peng–Robinson equation of state with the fluid compositions that were predicted by the TAMOC simulation at each time point.

S13 References

(1) Pesch, S.; Jaeger, P.; Jaggi, A.; Malone, K.; Hoffmann, M.; Krause, D.; Oldenburg, T. B. P.; Schlüter, M. Rise Velocity of Live-Oil Droplets in Deep-Sea Oil Spills. *Environ. Eng. Sci.* **2018**, *35* (4), 289–299. https://doi.org/10.1089/ees.2017.0319.

(2) Gros, J.; Socolofsky, S. A.; Dissanayake, A. L.; Jun, I.; Zhao, L.; Boufadel, M. C.; Reddy, C. M.; Arey, J. S. Petroleum Dynamics in the Sea and Influence of Subsea Dispersant Injection during *Deepwater Horizon*. *PNAS* **2017**, 201612518. https://doi.org/10.1073/pnas.1612518114.

(3) Gros, J.; Reddy, C. M.; Nelson, R. K.; Socolofsky, S. A.; Arey, J. S. Simulating Gas−Liquid−Water Partitioning and Fluid Properties of Petroleum under Pressure: Implications for Deep-Sea Blowouts. *Environ. Sci. Technol.* **2016**, *50* (14), 7397–7408. https://doi.org/10.1021/acs.est.5b04617.

(4) Dissanayake, A. L.; Gros, J.; Socolofsky, S. A. Integral Models for Bubble, Droplet, and Multiphase Plume Dynamics in Stratification and Crossflow. *Environ Fluid Mech* **2018**, 1–36. https://doi.org/10.1007/s10652-018-9591-y.

(5) Jun, I. A Numerical Model for Hydrocarbon Bubbles from Natural Seeps within Hydrate Stability Zone. Ph.D. Dissertation, Texas A&M University, College Station, Texas, 2018.

(6) Leonte, M.; Wang, B.; Socolofsky, S. A.; Mau, S.; Breier, J. A.; Kessler, J. D. Using Carbon Isotope Fractionation to Constrain the Extent of Methane Dissolution into the Water Column Surrounding

a Natural Hydrocarbon Gas Seep in the Northern Gulf of Mexico. *Geochem. Geophy. Geosy.* **2018**, *19* (11), 4459–4475. https://doi.org/10.1029/2018GC007705.

(7) Gros, J.; Dissanayake, A. L.; Daniels, M. M.; Barker, C. H.; Lehr, W.; Socolofsky, S. A. Oil Spill Modeling in Deep Waters: Estimation of Pseudo-Component Properties for Cubic Equations of State from Distillation Data. *Mar. Pollut. Bull.* **2018**, *137*, 627–637. https://doi.org/10.1016/j.marpolbul.2018.10.047.

(8) Gros, J.; Schmidt, M.; Dale, A. W.; Linke, P.; Vielstädte, L.; Bigalke, N.; Haeckel, M.; Wallmann, K.; Sommer, S. Simulating and Quantifying Multiple Natural Subsea CO_2 Seeps at Panarea Island (Aeolian Islands, Italy) as a Proxy for Potential Leakage from Subseabed Carbon Storage Sites. *Environ. Sci. Technol.* **2019**, *53* (17), 10258–10268. https://doi.org/10.1021/acs.est.9b02131.

(9) Socolofsky, S. A.; Dissanayake, A. L.; Jun, I.; Gros, J.; Arey, J. S.; Reddy, C. M. Texas A&M Oilspill Calculator (TAMOC) Modeling Suite for Subsea Spills. In *Proceedings of the Thirty-Eighth AMOP Technical Seminar*; Environment Canada: Ottawa, 2015; pp 153–168.

(10) McGinnis, D. F.; Greinert, J.; Artemov, Y.; Beaubien, S. E.; Wüest, A. Fate of Rising Methane Bubbles in Stratified Waters: How Much Methane Reaches the Atmosphere? *J. Geophys. Res.* **2006**, *111* (C9), C09007. https://doi.org/10.1029/2005JC003183.

(11) King, M. B. *Phase Equilibrium in Mixtures*; Danckwerts, P. V., Ed.; International series of monographs in chemical engineering; Pergamon press: Oxford, 1969.

(12) Dhima, A.; de Hemptinne, J.-C.; Jose, J. Solubility of Hydrocarbons and CO_2 Mixtures in Water under High Pressure. *Ind. Eng. Chem. Res.* **1999**, *38* (8), 3144–3161. https://doi.org/10.1021/ie980768g.

(13) Schwarzenbach, R. P.; Gschwend, P. M.; Imboden, D. M. *Environmental Organic Chemistry*, 2nd ed.; John Wiley & Sons, Inc.: Hoboken, 2003.

(14) Sander, R. Compilation of Henry's Law Constants, Version 3.99. *Atmos. Chem. Phys. Discuss.* **2014**, *14* (21), 29615–30521. https://doi.org/10.5194/acpd-14-29615-2014.

(15) Krichevsky, I. R.; Kasarnovsky, J. S. Thermodynamical Calculations of Solubilities of Nitrogen and Hydrogen in Water at High Pressures. *J. Am. Chem. Soc.* **1935**, *57* (11), 2168–2171. https://doi.org/10.1021/ja01314a036.

(16) Peng, D.-Y.; Robinson, D. B. A New Two-Constant Equation of State. *Ind. Eng. Chem. Fund.* **1976**, *15* (1), 59–64. https://doi.org/10.1021/i160057a011.

(17) Ahmed, T. *Reservoir Engineering Handbook*, 4th ed.; Elsevier: Burlington, 2010.

(18) Robinson, D. B.; Peng, D.-Y. *The Characterization of the Heptanes and Heavier Fractions for the GPA Peng-Robinson Programs*; Research Report 28; Gas Processors Association: Tulsa, 1978.

(19) Gros, J. Investigating the Fate of Petroleum Fluids Released in the Marine Environment with Comprehensive Two-Dimensional Gas Chromatography and Transport Models. Ph.D. Dissertation, École polytechnique fédérale de Lausanne, Lausanne, 2016.

(20) Clift, R.; Grace, J. R.; Weber, M. E. *Bubbles, Drops, and Particles*; Academic Press: New York, 1978.

(21) Kumar, A.; Hartland, S. Correlations for Prediction of Mass Transfer Coefficients in Single Drop Systems and Liquid–Liquid Extraction Columns. *Chem. Eng. Res. Des.* **1999**, *77* (5), 372–384. https://doi.org/10.1205/026387699526359.

(22) Johnson, A. I.; Besik, F.; Hamielec, A. E. Mass Transfer from a Single Rising Bubble. *The Canadian Journal of Chemical Engineering* **1969**, *47*, 559–564.

(23) Gill, A. E. *Atmosphere-Ocean Dynamics*; International Geophysics Series; Academic Press: New York, 1982.

(24) Sharqawy, M. H.; Lienhard, J. H.; Zubair, S. M. Thermophysical Properties of Seawater: A Review of Existing Correlations and Data. *Desalin. Water Treat.* **2010**, *16* (1–3), 354–380. https://doi.org/10.5004/dwt.2010.1079.

(25) McCain, W. D., Jr. *The Properties of Petroleum Fluids*, 2nd ed.; PennWell: Tulsa, 1990.

(26) Hayduk, W.; Laudie, H. Prediction of Diffusion Coefficients for Nonelectrolytes in Dilute Aqueous Solutions. *AIChE J.* **1974**, *20* (3), 611–615. https://doi.org/10.1002/aic.690200329.
(27) Pedersen, K. S.; Christensen, P. L.; Shaikh, J. A. *Phase Behavior of Petroleum Reservoir Fluids*, 2nd ed.; CRC Press: Boca Raton, 2014.
(28) Danesh, A. *PVT and Phase Behaviour of Petroleum Reservoir Fluids*, Elsevier.; Developments in Petroleum Science; Amsterdam, 1998.
(29) Firoozabadi, A.; Ramey, H. J. Surface Tension of Water-Hydrocarbon Systems at Reservoir Conditions. *J. Can. Petrol. Technol.* **1988**, *27* (03), 41–48. https://doi.org/10.2118/88-03-03.
(30) Poling, B., E.; Prausnitz, J. M.; O'Connell, J. P. *The Properties of Gases and Liquids*, 5th ed.; McGraw-Hill, 2001.
(31) Wang, B.; Socolofsky, S. A.; Lai, C. C. K.; Adams, E. E.; Boufadel, M. C. Behavior and Dynamics of Bubble Breakup in Gas Pipeline Leaks and Accidental Subsea Oil Well Blowouts. *Mar. Pollut. Bull.* **2018**, *131, Part A*, 72–86. https://doi.org/10.1016/j.marpolbul.2018.03.053.
(32) Zhao, L.; Boufadel, M. C.; Socolofsky, S. A.; Adams, E.; King, T.; Lee, K. Evolution of Droplets in Subsea Oil and Gas Blowouts: Development and Validation of the Numerical Model VDROP-J. *Mar. Pollut. Bull.* **2014**, *83* (1), 58–69. https://doi.org/10.1016/j.marpolbul.2014.04.020.
(33) Johansen, Ø.; Brandvik, P. J.; Farooq, U. Droplet Breakup in Subsea Oil Releases – Part 2: Predictions of Droplet Size Distributions with and without Injection of Chemical Dispersants. *Mar. Pollut. Bull.* **2013**, *73* (1), 327–335. https://doi.org/10.1016/j.marpolbul.2013.04.012.
(34) Li, Z.; Spaulding, M.; French McCay, D.; Crowley, D.; Payne, J. R. Development of a Unified Oil Droplet Size Distribution Model with Application to Surface Breaking Waves and Subsea Blowout Releases Considering Dispersant Effects. *Mar. Pollut. Bull.* **2017**, *114* (1), 247–257. https://doi.org/10.1016/j.marpolbul.2016.09.008.
(35) Ryerson, T. B.; Camilli, R.; Kessler, J. D.; Kujawinski, E. B.; Reddy, C. M.; Valentine, D. L.; Atlas, E.; Blake, D. R.; de Gouw, J.; Meinardi, S.; Parrish, D. D.; Peischl, J.; Seewald, J. S.; Warneke, C. Chemical Data Quantify *Deepwater Horizon* Hydrocarbon Flow Rate and Environmental Distribution. *PNAS* **2012**, *109* (50), 20246–20253. https://doi.org/10.1073/pnas.1110564109.
(36) BP Gulf Science Data. Chemistry data associated with water column samples collected in the Gulf of Mexico from May 2010 through July 2012. Available at: https://data.gulfresearchinitiative.org/data/BP.x750.000:0016#distributionInfo (accessed Aug 3, 2017).
(37) Reddy, C. M.; Arey, J. S.; Seewald, J. S.; Sylva, S. P.; Lemkau, K. L.; Nelson, R. K.; Carmichael, C. A.; McIntyre, C. P.; Fenwick, J.; Ventura, G. T.; Mooy, B. A. S. V.; Camilli, R. Composition and Fate of Gas and Oil Released to the Water Column during the *Deepwater Horizon* Oil Spill. *PNAS* **2012**, *109* (50), 20229–20234. https://doi.org/10.1073/pnas.1101242108.
(38) Diercks, A.-R.; Highsmith, R. C.; Asper, V. L.; Joung, D.; Zhou, Z.; Guo, L.; Shiller, A. M.; Joye, S. B.; Teske, A. P.; Guinasso, N.; Wade, T. L.; Lohrenz, S. E. Characterization of Subsurface Polycyclic Aromatic Hydrocarbons at the *Deepwater Horizon* Site. *Geophys. Res. Lett.* **2010**, *37* (20). https://doi.org/10.1029/2010GL045046.
(39) Pesch, S.; Schlüter, M.; Aman, Z. M.; Malone, K.; Krause, D.; Paris, C. B. Behavior of Rising Droplets and Bubbles: Impact on the Physics of Deep-Sea Blowouts and Oil Fate. In *Deep Oil Spills: Facts, Fate, and Effects*; Murawski, S. A., Ainsworth, C. H., Gilbert, S., Hollander, D. J., Paris, C. B., Schlüter, M., Wetzel, D. L., Eds.; Springer International Publishing: Cham, 2020; pp 65–82. https://doi.org/10.1007/978-3-030-11605-7_5.
(40) Spaulding, M.; Mendelsohn, D.; Crowley, D.; Li, Z.; Bird, A. *Technical Reports for* Deepwater Horizon *Water Column Injury Assessment WC_TR.13: Application of OILMAP DEEP to the* Deepwater Horizon *Blowout*; RPS ASA: South Kingstown, 2015; p 368.

(41) Aliseda, A.; Bommer, P.; Espina, P.; Flores, O.; Lasheras, J. C.; Lehr, B.; Leifer, I.; Possolo, A.; Riley, J.; Savas, O.; Shaffer, F.; Wereley, S.; Yapa, P. *Deepwater Horizon Release Estimate by PIV*; National Incident Command Flow Rate Technical Group, 2010; p 215.
(42) French McCay, D.; Jayko, K.; Li, Z.; Horn, M.; Kim, Y.; Isaji, T.; Crowley, D.; Spaulding, M.; Decker, L.; Turner, C.; Zamorski, S.; Fontenault, J.; Shmookler, R.; Rowe, J. *Technical Reports for* Deepwater Horizon *Water Column Injury Assessment WC_TR.14: Modeling Oil Fate and Exposure Concentrations in the Deepwater Plume and Rising Oil Resulting from the* Deepwater Horizon *Oil Spill*; RPS ASA: South Kingstown, 2015; p 536.
(43) Testa, J. M.; Adams, E. E.; North, E. W.; Ruoying, H. Modeling the Influence of Deep Water Application of Dispersants on the Surface Expression of Oil: A Sensitivity Study. *J. Geophys. Res.-Oceans* **2016**, *121* (8), 5995–6008. https://doi.org/10.1002/2015JC011571.
(44) Zhao, L.; Boufadel, M. C.; Adams, E.; Socolofsky, S. A.; King, T.; Lee, K.; Nedwed, T. Simulation of Scenarios of Oil Droplet Formation from the *Deepwater Horizon* Blowout. *Mar. Pollut. Bull.* **2015**, *101* (1), 304–319. https://doi.org/10.1016/j.marpolbul.2015.10.068.
(45) Xue, X.; Katz, J. Formation of Compound Droplets during Fragmentation of Turbulent Buoyant Oil Jet in Water. *J. Fluid Mech.* **2019**, *878*, 98–112. https://doi.org/10.1017/jfm.2019.645.
(46) Römer, M.; Hsu, C.-W.; Loher, M.; MacDonald, I. R.; dos Santos Ferreira, C.; Pape, T.; Mau, S.; Bohrmann, G.; Sahling, H. Amount and Fate of Gas and Oil Discharged at 3400 m Water Depth From a Natural Seep Site in the Southern Gulf of Mexico. *Front. Mar. Sci.* **2019**, *6*. https://doi.org/10.3389/fmars.2019.00700.
(47) Pilson, M. E. Q. *An Introduction to the Chemistry of the Sea*, 2nd ed.; Cambridge University Press: Cambridge, 2013.
(48) Wang, B.; Lai, C. C. K.; Socolofsky, S. A. Mean Velocity, Spreading and Entrainment Characteristics of Weak Bubble Plumes in Unstratified and Stationary Water. *J. Fluid Mech.* **2019**, *874*, 102–130. https://doi.org/10.1017/jfm.2019.461.
(49) Vielstädte, L.; Karstens, J.; Haeckel, M.; Schmidt, M.; Linke, P.; Reimann, S.; Liebetrau, V.; McGinnis, D. F.; Wallmann, K. Quantification of Methane Emissions at Abandoned Gas Wells in the Central North Sea. *Mar. Petrol. Geol.* **2015**, *68*, 848–860. https://doi.org/10.1016/j.marpetgeo.2015.07.030.
(50) Sellami, N.; Dewar, M.; Stahl, H.; Chen, B. Dynamics of Rising CO_2 Bubble Plumes in the QICS Field Experiment: Part 1 – The Experiment. *Int. J. Greenh. Gas Con.* **2015**, *38*, 44–51. https://doi.org/10.1016/j.ijggc.2015.02.011.
(51) Riazi, M. R. *Characterization and Properties of Petroleum Fractions*; ASTM International, 2005.
(52) Naqvi, S. W. A.; Bange, H. W.; Farías, L.; Monteiro, P. M. S.; Scranton, M. I.; Zhang, J. Marine Hypoxia/Anoxia as a Source of CH_4 and N_2O. *Biogeosciences* **2010**, *7* (7), 2159–2190. https://doi.org/10.5194/bg-7-2159-2010.
(53) Fan, L.-S.; Tsuchiya, K. *Bubble Wake Dynamics in Liquids and Liquid–Solid Suspensions*; Elsevier, 1990. https://doi.org/10.1016/C2009-0-24002-5.
(54) Fan, L.-S.; Yang, G. Q.; Lee, D. J.; Tsuchiya, K.; Luo, X. Some Aspects of High-Pressure Phenomena of Bubbles in Liquids and Liquid–Solid Suspensions. *Chem. Eng. Sci.* **1999**, *54* (21), 4681–4709. https://doi.org/10.1016/S0009-2509(99)00348-6.
(55) Schlüter, M.; Pesch, S. Expansion of Gas-Saturated Crude Oil Droplets, 2017. https://doi.org/10.7266/N79885GB.
(56) Oldenburg, T. B. P.; Jaeger, P.; Gros, J.; Socolofsky, S. A.; Pesch, S.; Radović, J. R.; Jaggi, A. Physical and Chemical Properties of Oil and Gas Under Reservoir and Deep-Sea Conditions. In *Deep Oil Spills: Facts, Fate, and Effects*; Murawski, S. A., Ainsworth, C. H., Gilbert, S., Hollander, D. J., Paris, C. B., Schlüter, M., Wetzel, D. L., Eds.; Springer International Publishing: Cham, 2020; pp 25–42. https://doi.org/10.1007/978-3-030-11605-7_3.

(57) Witherspoon, P. A.; Bonoli, L. Correlation of Diffusion Coefficients for Paraffin, Aromatic, and Cycloparaffin Hydrocarbons in Water. *Ind. Eng. Chem. Fund.* **1969**, *8* (3), 589–591. https://doi.org/10.1021/i160031a038.

(58) Guo, H.; Chen, Y.; Lu, W.; Li, L.; Wang, M. In Situ Raman Spectroscopic Study of Diffusion Coefficients of Methane in Liquid Water under High Pressure and Wide Temperatures. *Fluid Phase Equilibr.* **2013**, *360*, 274–278. https://doi.org/10.1016/j.fluid.2013.09.051.

(59) Sachs, W. The Diffusional Transport of Methane in Liquid Water: Method and Result of Experimental Investigation at Elevated Pressure. *J. Petrol. Sci. Eng.* **1998**, *21* (3), 153–164. https://doi.org/10.1016/S0920-4105(98)00048-5.

(60) Ho, T. A.; Criscenti, L. J.; Wang, Y. Nanostructural Control of Methane Release in Kerogen and Its Implications to Wellbore Production Decline. *Scientific Reports* **2016**, *6* (1), 1–9. https://doi.org/10.1038/srep28053.

(61) *Aerial Observations of Oil at Sea*; HAZMAT; 96–7; National Oceanic and Atmospheric Administration, Office of Ocean Resources Conservation and Assessment, Hazardous Materials Response and Assessment Division, Modeling and Simulation Studies Branch: Seattle, Washington, U.S.A., 1996.

(62) Socolofsky, S. A.; Adams, E. E.; Sherwood, C. R. Formation Dynamics of Subsurface Hydrocarbon Intrusions Following the *Deepwater Horizon* Blowout. *Geophys. Res. Lett.* **2011**, *38* (9), L09602. https://doi.org/10.1029/2011GL047174.

(63) Camilli, R.; Reddy, C. M.; Yoerger, D. R.; Mooy, B. A. S. V.; Jakuba, M. V.; Kinsey, J. C.; McIntyre, C. P.; Sylva, S. P.; Maloney, J. V. Tracking Hydrocarbon Plume Transport and Biodegradation at *Deepwater Horizon*. *Science* **2010**, *330* (6001), 201–204. https://doi.org/10.1126/science.1195223.

(64) Hazen, T. C.; Dubinsky, E. A.; DeSantis, T. Z.; Andersen, G. L.; Piceno, Y. M.; Singh, N.; Jansson, J. K.; Probst, A.; Borglin, S. E.; Fortney, J. L.; Stringfellow, W. T.; Bill, M.; Conrad, M. E.; Tom, L. M.; Chavarria, K. L.; Alusi, T. R.; Lamendella, R.; Joyner, D. C.; Spier, C.; Baelum, J.; Auer, M.; Zemla, M. L.; Chakraborty, R.; Sonnenthal, E. L.; D'haeseleer, P.; Holman, H.-Y. N.; Osman, S.; Lu, Z.; Nostrand, J. D. V.; Deng, Y.; Zhou, J.; Mason, O. U. Deep-Sea Oil Plume Enriches Indigenous Oil-Degrading Bacteria. *Science* **2010**, *330* (6001), 204–208. https://doi.org/10.1126/science.1195979.

(65) Fingas, M. Chapter 15. Deepwater Horizon Well Blowout Mass Balance. In *Oil Spill Science and Technology*; Gulf Professional Publishing (Elsevier): Cambridge (USA) and Oxford (UK), 2017; p 1078.

(66) Socolofsky, S. A.; Gros, J.; Zhao, L.; Boufadel, M. C. Research Version of the Texas A&M Oil Spill (Outfall) Calculator (TAMOC) and Input Files, 2016. https://doi.org/10.7266/n7df6p8r.

(67) Davis, C. S.; Loomis, N. *Deepwater Horizon Oil Spill (DWHOS) Water Column Technical Working Group, Image Data Processing Plan: Holocam, Description of Data Processing Methods Used to Determine Oil Droplet Size Distributions from in Situ Holographic Imaging during June 2010 on Cruise M/V Jack Fitz 3.*; 2014.

(68) Li, Z.; Bird, A.; Payne, J.; Vinhateiro, N.; Kim, Y.; Davis, C.; Loomis, N. *Technical Reports for* Deepwater Horizon *Water Column Injury Assessment: Oil Particle Data from the* Deepwater Horizon *Oil Spill*; RPS ASA: South Kingstown, 2015.

(69) Paris, C. B.; Hénaff, M. L.; Aman, Z. M.; Subramaniam, A.; Helgers, J.; Wang, D.-P.; Kourafalou, V. H.; Srinivasan, A. Evolution of the Macondo Well Blowout: Simulating the Effects of the Circulation and Synthetic Dispersants on the Subsea Oil Transport. *Environ. Sci. Technol.* **2012**, *46* (24), 13293–13302. https://doi.org/10.1021/es303197h.

(70) North, E. W.; Adams, E. E.; Schlag, Z.; Sherwood, C. R.; He, R.; Hyun, K. H.; Socolofsky, S. A. Simulating Oil Droplet Dispersal from the *Deepwater Horizon* Spill with a Lagrangian Approach. In *Monitoring and Modeling the Deepwater Horizon Oil Spill: A Record-Breaking Enterprise*; Liu, Y., Macfadyen, A., Ji, Z.-G., Weisberg, R. H., Eds.; Geophysical Monograph Series; 2013.

(71) Lee, J. H. W.; Cheung, V. Generalized Lagrangian Model for Buoyant Jets in Current. *J. Environ. Eng.* **1990**, *116* (6), 1085–1106. https://doi.org/10.1061/(ASCE)0733-9372(1990)116:6(1085).
(72) Infelta, P.; Graetzel, M. *Thermodyamique: Principe et applications*; BrownWalker Press: Boca Raton,Florida, 2006.
(73) Zick, A. A. *Equation-of-State Fluid Characterization and Analysis of the Macondo Reservoir Fluids*; Expert report prepared on behalf of the United States TREX-011490R; 2013.
(74) Zick, A. A. *Expert Rebuttal Report*; prepared on behalf of the United States TREX-011491R; 2013.
(75) McNutt, M. K.; Camilli, R.; Crone, T. J.; Guthrie, G. D.; Hsieh, P. A.; Ryerson, T. B.; Savas, O.; Shaffer, F. Review of Flow Rate Estimates of the *Deepwater Horizon* Oil Spill. *PNAS* **2012**, *109* (50), 20260–20267. https://doi.org/10.1073/pnas.1112139108.